CIRCULATION COPY
SUBJECT TO RECALL
IN TWO WEEKS

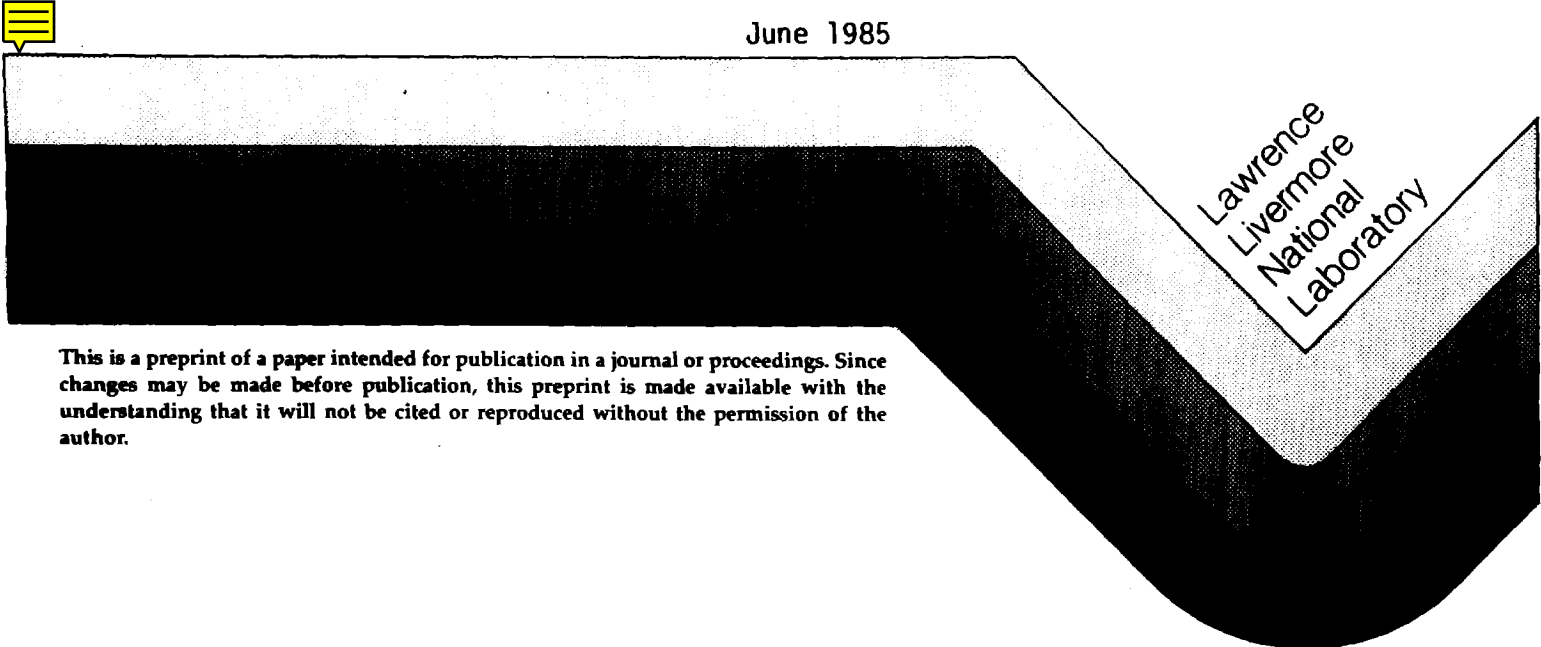# STABILITY OF FIELD REVERSED ION RINGS

Alex Friedman
Lawrence Livermore National Laboratory

R. N. Sudan
Laboratory of Plasma Studies
Cornell University, Ithaca NY 14853

Jacques Denavit
Lawrence Livermore National Laboratory

This paper was prepared for submittal to
The Physics of Fluids

June 1985

DISCLAIMER

Stability of Field Reversed Ion Rings *

Alex Friedman

*Lawrence Livermore National Laboratory,
University of California, Livermore CA 94550*

R. N. Sudan

*Laboratory of Plasma Studies
Cornell University, Ithaca NY 14853*

and

Jacques Denavit

*Lawrence Livermore National Laboratory,
University of California, Livermore CA 94550*

ABSTRACT

Studies of the low frequency stability of field reversed ion rings in a dense uniform plasma background have been carried out using a linearized 3d hybrid simulation model. For a moderately thick ring with aspect ratio on the order of 4:1, the azimuthal mode number $l = 1$ radial mode (MHD precession) is observed to be stable, due to the favorable field gradient arising from image currents in the outer wall. The $l = 1$ axial (tilt) mode is unstable for the parameters chosen, as are the $l = 2$ radial and axial (kink) modes, and the $l = 3$ radial mode. All other modes are observed to be either stable or very weakly unstable; numerical difficulties arising from the local instability of individual orbits in the equilibrium field make it difficult to examine modes with small growth rates. The structures of the various unstable modes range from near-rigid to quite complicated in displacement pattern. Some preliminary evidence for the existence of betatron resonance – driven instablilities is noted.

1. INTRODUCTION

This paper describes investigations of the low frequency stability of field reversed ion rings, carried out using time-dependent computer simulation methods. These rings are comprised of a large number of energetic ions gyrating in an externally imposed magnetic field, and have sufficient density that the total (external + self) magnetic field is reversed over a significant volume. Such configurations are of interest because they contain a region of closed flux surfaces, and in fact for the rings considered, closed field lines. The geometry of such a system is depicted in fig. 1.

The field reversed ion ring concept is the basis for the ion ring compressor fusion reactor proposal,[1,2] a development of the "Astron" device;[3] related schemes are the field reversed mirror,[4] the spheromak,[5] and the reversed field theta pinch.[6] In these last three, the bulk of the ions do not execute axis-encircling orbits, but rather are carried around in azimuth by a drift motion. Furthermore, a hybrid ion ring – spheromak in which a fraction of the azimuthal current is carried by axis encircling ions has also been suggested[7] as a means for improving the spheromak's stability to tilt and other modes. The physical configuration we consider is quite different. Here, we examine the stability of very energetic rings in a pressureless background plasma which supports no equilibrium current.

The stability of field-reversed rings and layers to high-frequency modes has been studied effectively through theoretical analyses, because these modes involve short wavelengths and simplified geometries preserve the essential physics of the mode.[8] With respect to low-frequency stability, results on precessional[9,10,11,12] and tearing[13,14] modes have been available for some time. The stability of a plasma confined in the closed field lines of a ring (assumed to be rigidly fixed) has also been treated using the magnetohydrodynamic energy principle.[15] The kink modes of beams and rings have been examined,[16] and an "energy principle" based on the Vlasov equation has been developed to treat the general low-frequency stability of axisymmetric field-reversed equilibria of arbitrary ion gyroradius.[17]

These analyses have treated "bicycle-tire" (small inverse aspect ratio) and long-layer equilibria, such approximations being necessary to render the analysis tractable. Some general implication of this work are that "thick" bicycle tires would be most stable to kink modes, in the sense that stability criteria are satisfied when the parameters of a ring with unit aspect ratio are inserted into the thin ring theory which, however, cannot rigorously be applied in this regime. Similarly, it has been found that infinite layers are stable to precessional and kink modes of sufficiently short axial wavelength.[17] Since a maximum wavelength is imposed by finite layer length, the implication is that

finite-length layers might be stable. However, the analysis does not include the destabilizing effect of fieldline curvature at the layer ends. Nonetheless, it is conjectured that a ring with aspect ratio of order unity will represent the most stable configuration; such an aspect ratio is observed in the electron ring experiments.[18]

Theoretical analyses have been unable to reach this regime, as no simple analytical equilibria are known, and approximate treatments are difficult since the inverse aspect ratio cannot be used as an expansion parameter. However, Vlasov equilibria for rings and mirror plasmas have been found by computational methods.[19,20,21] Thus, one possible approach to the low-frequency stability problem would be to apply a normal mode analysis or an energy principle as in theoretical treatments, solving the resulting equations numerically. In our present approach, we have chosen instead to directly apply particle-in-cell and fluid simulation techniques to the low-frequency stability problem.

The simulation program developed for this study is a linearized three dimensional hybrid code called RINGHYBRID.[22] This program models a strong ion ring (represented by discrete simulation superparticles) in a plasma consisting of a cold, uniform background ion component and an inertialess electron component of density appropriate for local quasineutrality (both modeled by fluid equations). To lowest order the ring particles are axisymmetric rings having r,z location and r,θ,z velocity coordinates. First order perturbations having azimuthal mode number l are considered, so that each particle k is deformed by an infinitesimal displacement $(\varepsilon_{rk}\hat{r}+\varepsilon_{\theta k}\hat{\theta}+\varepsilon_{zk}\hat{z})\exp(il\theta)$, where $\underline{\varepsilon}$ is complex. Fields and currents are represented by axisymmetric zero order parts, plus first order parts varying as $\exp(il\theta)$, defined on an Eulerian mesh in the r-z plane. Since each simulation particle represents an infinite set of real particles lying on a nonaxisymmetric ring, a considerable economy of computation relative to a nonlinear 3D code is possible. Meaningful runs can be made using a few thousand particles; however, the processing of each particle is much more complicated than in a nonliner code.

Effects of "stochastic" single-particle orbits are observed in these simulations; due to the local instability of particle trajectories, neighboring orbits diverge exponentially with time. This leads to a loss of left-right symmetry in the zero order motion; however, in the linearized simulation the associated "growth" can sometimes be sufficiently rapid as to mask the collective modes which are the true objects of study. The growth arises because $\underline{\varepsilon}$ measures the separation between two trajectories (those of a point on the unperturbed particle and a point on the deformed particle) which are, due to the linearization, forever infinitesimally close togther. This effect has been described in detail elsewhere.[23]

The stability properties of some field-reversed ion ring equilibria
which do not exhibit rapid orbit separation have been examined. One
moderately thick ion ring is studied in detail. This equilibrium is
stable to the MHD precession because a wall is present at finite radius;
kink mode behavior is observed to agree closely with predictions based
upon thin-ring theory. Some evidence for the possible existence of
betatron-resonance instabilities is noted.

The plan of this paper is as follows: in section II the relevant
theoretical treatments of field reversed ion ring stability in a
background plasma are reviewed. In section III the simulation model,
and the effects of stochastic orbits upon its performance, are described
briefly. In section IV the equilibrium of a strong ion ring is
described in detail, and the stability of this ring with respect to
perturbations with various values of ℓ is discussed. The structures of
the unstable eigenmodes are also described. In section V this work is
summarized, and conclusions drawn.

II. APPLICABLE THEORIES

The theory of field reversed particle ring stability has recently
been reviewed in considerable detail[24]. Here we summarize those
elements of the theory which will aid our understanding of the
simulation results.

A. Rigid perturbation model

The first works on the magnetohydrodynamic stability of Astron
configurations invoked the restrictive assumption that the particle
layer could be treated as rigid and immobile.[15] The next development
was consideration of a beam segmented into cross-sections which executed
rigid transverse motions, with the shape of the cross-sections
preserved. This model, which is suitable for kink modes, was applied by
Lee to straight beam systems[25], and by Lovelace to thin ion rings in a
background plasma with $|\omega| << |\omega_{e_i}|$.[16] An heuristic model which yields
similar results was also developed by Humphries.[26] As in the RINGHYBRID
simulation model, in Lovelace's work the ring is assumed to be embedded
in a dense, pressureless background plasma, and there is no equilibrium
plasma current nor charge separation. In addition, the aspect ratio R/a
of the ring is assumed to be large ("bicycle tire approximation"). The
rigid kink modes are the primary objects of study, with poloidal mode
number $m = \pm 1$, toroidal number n (called ℓ in our simulations) nonzero.

The development of Lovelace's theory is as follows. First, the plasma response to low-frequency kink-like beam perturbations is found, and a basic energy equation is derived for beam-plasma perturbations. The dynamics of the beam perturbation itself are then derived, and related to the plasma perturbation.

For the linear beam case (most of the development), the coordinate system is (r,θ,s), where s is the toroidal coordinate, r the poloidal (minor) radius, and θ the poloidal angle. Perturbations have the structure $\exp(im\theta+iks)$, where $k = n/R$. The background plasma (of density n_p) fills the region occupied by the beam (of density n_b) out to radius r_w of the conducting vessel wall. In the bicycle tire limit only the self-field is important, and $\underline{B} = B_\theta(r)\hat{\theta}$.

The analysis uses Maxwell's equations and the MHD equations, retaining the correction term $qn_b\underline{\delta E}$ in the momentum equation since n_b/n_p is small but not negligible.

Treatment of the beam dynamics is simplified by relating displacements $\underline{\epsilon}$ of the beam center-of-mass (not to be confused with the $\underline{\epsilon}_k$ used to describe the displacement of simulation particle k in the code) to the field perturbations; the beam current density perturbations are in turn expressed in terms of $\underline{\epsilon}$.

In the linearized particle equations of motion, the first order electric field is neglected (essentially because $n_b/n_p \ll 1$). Assuming low frequency perturbations with $|\omega| < v_A/a$ and $|ka| \gtrsim a/R \gg |v_A/\bar{v}_s|$, and a uniform beam velocity $\bar{v}_s$ so that $d/dt \sim ikv_s$ (thus excluding conventional precession and $\ell = 0$ modes from study), the displacement $\underline{\epsilon}$ is related to the (averaged over poloidal radius) first order field by:

$$\epsilon_x = (q\bar{v}_s/m_b c)[(k\bar{v}_s)^2 - \omega_\beta^2]^{-1}<\delta B_y>$$

$$\epsilon_y = im\epsilon_x \quad \text{(for the "helical" kink).}$$

(1)

Here the effective betatron frequency is defined by:

$$\omega_\beta^2 = (2\pi q\bar{v}_s/m_b c^2) \int d^3x \, J_b^2 \, / \int d^3x \, J_b$$

$$\approx (2\pi q\bar{v}_s/m_b c^2)<J_b>_r,$$

(2)

(the subscript r denotes an average over poloidal radius). The first of these forms is evaluated as a diagnostic in RINGHYBRID. The resonance factor in square brackets in eq. (1) is presumed to be limited by spreads of v_s (toroidal velocity) with r and by the thermal spread of v_s; thus, the "resonance region" $(k\bar{v}_s)^2 \sim \omega_\beta^2$ is excluded from study.

A sufficient condition for stability is $|k\bar{v}_s| > \omega_\beta$ for all relevant wavenumbers. This is equivalent to requiring that the wavelength $|\lambda| < \lambda_\beta = 2\pi|\bar{v}_s|/\omega_\beta$. Since $k = 0$ is excluded, λ must be less than $2\pi R$.

and a sufficient condition for stability is $\lambda_\beta > 2\pi R$, or equivalently $\tau_\beta > \tau_g$, where the betatron period $\tau_\beta = 2\pi/\omega_\beta$ and the gyration period $\tau_g = 2\pi R/\bar{v}_s$. This sufficient stability condition can also be expressed as $4\pi n_b m_b \bar{v}_s^2/B_{ext}^2 = \beta_\theta < 2/g^2$, where β_θ is the ratio of the directed beam kinetic energy density to the energy density of the external magnetic field, and g is a dimensionless factor of order unity given by $g = |R\Omega_{ext}/\bar{v}_s|$ (≈ 1 for a weak ring), where Ω_{ext} is the external-field gyration frequency.

When the sufficient condition for stability is satisfied, the self-field betatron wavelength of a beam particle is longer than the maximum allowable wavelength ($2\pi R$), and the beam displacement in response to a magnetic field perturbation δB is opposite in direction to the $\underline{v} \times \delta B$ force on a single particle; when the sufficient condition is not satisfied, the beam displacement is in the direction of the Lorentz force, and δB is enhanced. Lovelace notes that the condition for unity field reversal on axis (field cancellation) is $\beta_\theta > (2/\pi g)(R/a)^2$; this is "compatible" with the stability criterion when $(R/a) < (\pi/g)^{1/2}$, which however violates the assumption of large aspect ratio.

Note that these stability criteria are independent of the wall radius (except for the dependence in g) and plasma density, but that the true stability threshold might have a more complicated dependence (these criteria are sufficient but not necessary for stability). Furthermore, Lovelace computes an upper bound to the growth rate which is very roughly proportional to $(v_A/a)(\bar{v}_\zeta/\Delta v_\zeta)^{1/2}$, where Δv_ζ is the spread in beam velocity.

The second model considered is one where the toroidal nature of the ring is taken into account.[16] This case is of greater direct relevance to the RINGHYBRID simulations. Toroidal effects break the $m = \pm 1$ degeneracy of the kink mode; normal modes become "axial" and "radial", and the above sufficient stability condition no longer implies stability of the $\ell = 1$ radial (MHD precession) mode.

The axial and radial modes have differing parity under the transformations (in RINGHYBRID's cylindrical coordinate system) $[r,\theta,(z-L/2)] \rightarrow [r,\theta,(L/2-z)]$, where L is the system length and the zero-order state is mirror symmetric about $z = L/2$. For the radial mode,

$$\varepsilon_{r,\theta} \rightarrow +\varepsilon_{r,\theta}, \quad \varepsilon_z \rightarrow -\varepsilon_z,$$

$$\delta B_{r,\theta} \rightarrow -\delta B_{r,\theta}, \quad \delta B_z \rightarrow +\delta B_z, \tag{3}$$

and the signs are reversed for the axial mode.

A sufficient stability criterion for the axial modes is

$$(\ell\Omega)^2 > \omega_\beta^2 + \omega_z^2. \tag{4}$$

where the axial __external-field__ betatron frequency is given by
$\omega_z = (-\eta_{ext})^{1/2}\Omega \ll 1$, and η_{ext} is the usual external field index,
$\eta_{ext} = (R/B_{ext})\partial B_{ext}/\partial r$; essentially this condition is the same as that
for the straight beam model.

For the radial modes, the stability condition is

$$(l\Omega)^2 > \omega_\beta^2 + \omega_r^2, \tag{5}$$

where the radial external-field betatron frequency is given by
$\omega_r = (1+\eta_{ext})^{1/2}\Omega \sim \Omega$ unless the wall is quite close (static
image-current fields are included in η_{ext}). For a significant departure
from a circular cross-section, the ω_β's in eqs. (4) and (5) would be
replaced by $\omega_{\beta z}$ and $\omega_{\beta r}$, respectively. Since for a strong ring $\Omega < \omega_\beta$,
for $l > 1$ the stability criterion for this model does not differ greatly
from that for the straight beam model (it is slightly harder to
satisfy). However, for $l = 1$ this sufficient condition for stability of
the "MHD precession" becomes $\omega_\beta^2 < -\eta_{ext}\Omega^2$, which is essentially
impossible to satisfy for a strong ion ring. A more detailed
treatment[11,12] shows that this stability criterion is too restrictive,
and that stability obtains when the external field index (including
image effects) is positive. Thus, a ring in a uniform external field
should be stable to low-frequency, nonresonant, $l = 1$ radial modes if
there is a radial wall at a finite distance.

B. Vlasov energy principle

A kinetic formalism for studying the low-frequency stability of
field-reversed equilibria was developed by Sudan and Rosenbluth in 1976,
with a detailed presentation appearing in 1979[17] (equations cited here
refer to the 1979 article). The contribution of the hot component (in
this case, the ion ring) to the perturbed current is described by the
Vlasov equation. The cold background plasma is described by fluid
equations, which are easily generalized to include plasma pressure and
currents. The basic idea underlying the treatment is similar to that of
the magnetohydrodynamic energy principle.[27]

There are several forms in which the extended energy principle may
be expressed, but the following is most convenient for many
applications:

$$\delta C = -\omega^2 K - \omega\mathcal{L} + \delta W_p + \delta W_b = 0, \tag{6}$$

where if $\delta C = 0$ for any perturbation with $\mathrm{Im}(\omega) > 0$ instability obtains.

For low enough real frequency, and neglecting particle resonance contributions in δW_b, a sufficient condition for stability is[17,24]

$$\delta W_p + \delta W_b - \omega K > 0. \tag{7}$$

Here

$$K = \tfrac{1}{2}\int d^3x\, n_i m_i |\xi|^2$$

$$\delta W_p = \tfrac{1}{2}\int d^3x\, |\delta \underline{B}|^2/4\pi$$

$$\delta W_b = \tfrac{1}{2}e_b^2\Omega\int d^3x\, d^3v\, |r\dot{\theta}\cdot\xi\times\underline{B}|^2\ \partial f_0/\partial H \tag{8}$$

$$\quad - \tfrac{1}{2}ie_b^2\Omega\int d^3x\, d^3v\, (\partial f_0/\partial H)\ g\ dg^*/dt$$

$$\mathscr{L} = -(ie_b/2c)\int d^3x\, n_b\ \xi^*\cdot\xi\times\underline{B}$$

Here, ξ is the electron displacement $= \xi_{\perp}$, $f_0 = f_0(H-\Omega P_\theta)$ is a rigid rotor equilibrium distribution, H is the (particle) Hamiltonian, Ω the (constant) angular velocity of the system, P_θ the (particle) canonical angular momentum, and the orbit integral along unperturbed trajectories g (not to be confused with Lovelace's g, above) is given by

$$g = \int_{-\infty}^{t} dt'\ \xi'\cdot\underline{v}'X\ \underline{B}'. \tag{9}$$

If the background plasma has pressure and carries a current, δW_p must be modified appropriately, as in the conventional MHD energy principle.

For the straight-beam model of the bicycle-tire ring, g is evaluated using the poloidal coordinate system (ρ,φ,s), where $s = R\theta$ is the toroidal coordinate. The Bennet pinch model is used:

$$B_\varphi(\rho) = \sqrt{2}(\rho/a)/(1+\rho/a)^2$$
$$n_b(\rho) = [1+(\rho/a)^2]^{-2} \tag{10}$$
$$J_s(\rho) = n_b e_b R\Omega.$$

A rough estimate of g is obtained by using for all particles the orbits appropriate to those near the beam axis (this would be exact for a square beam profile). A different treatment which directly invokes orbital stochasticity yields the same result if betatron resonances are neglected.[26] For these orbits the magnetic field strength varies linearly with ρ; letting $B_0 = B(\rho=a)$, the orbit integral g becomes:

$$g = -(B_0 v_0/a)\int_{-\infty}^{t} dt'\,\xi_\rho(t')\rho(t'). \tag{11}$$

where $\xi_\rho = \xi_\rho(\rho)\exp[i(m\varphi+ks-\omega t)]$ and $s = v_0 t$.

For the $(m = 1)$ kink mode (the primary object of study in our simulations), ξ_ρ is set to $(\zeta/a)\exp[i(\varphi + ks - \omega t)]$, where ζ is a constant ($|\underline{\delta B}|$ is minimized with respect to ξ_s). In the dense plasma limit, ω_r is set to zero because $n_b \ll n_p$. Setting $\omega = 0$, $\xi_\rho \approx$ constant, the result is[17]

$$\delta C = -\frac{k^2}{8\pi}\int d^3x\left(\rho\frac{dB}{d\rho}\right)^2 - \frac{k^2 v_0^2}{\omega_\beta^2 - k^2 v_0^2}\int d^3x\xi^2 J_0 B_0/a. \tag{12}$$

As in Lovelace's theory, $kv_0 = l\Omega > \omega_\beta$ is stabilizing, and furthermore the second term in the above equation is the more important of the two by a factor $v_0^2/a^2\omega_\beta^2$. Thus, the effective stability criterion agrees with that of the earlier work:

$$l\Omega > \omega_\beta. \tag{13}$$

with the same interpretation; a low frequency in the lab frame appears as $l\Omega$ in the beam frame, and particles do not respond coherently to perturbations above ω_β in their own frame.

C. Betatron resonance instabilities

A study of betatron resonance instabilities in field-reversed ion ring systems has been carried out by Finn and Sudan,[28] using the generalized energy principle. The modes involved are hydromagnetic modes of the background plasma, which are driven unstable by a resonant coupling with the beam when $\omega - l\Omega$ matches $\pm\omega_\beta$ of the resonant ions. Modes with phase velocity parallel to that of the ring (i.e. with negative energy in the beam frame) are unstable, while modes with opposite phase velocities are damped. The mechanism is similar to that associated with cyclotron instability and damping, with the relevant drift velocity in this case being due to the particle gyration and the resonance being with the betatron motion.

In the most general case, when some or all orbits are "ergodic" or "stochastic" on each (H, P_θ) surface in phase space, direct calculation of orbit integrals along unperturbed trajectories is difficult or impossible. However, by directly invoking this stochasticity, the beam contribution to the energy principle is expressed in terms of the power spectrum of orbital quantities, a positive definite function with peaks at the axial and radial betatron frequencies. The existence of a resonant (i.e. imaginary) part of the Hilbert transform of the power spectrum implies instability. The results are applied to a rigid kink

mode of the background plasma using the bicycle-tire approximation. For a fully reversed ring of moderate aspect ratio, i.e. when $(T/E)(R/a) \sim 1$, where T is the ring temperature and E its directed kinetic energy, hydromagnetically stable kink modes are driven unstable by the betatron resonances, and can grow on a hydromagnetic timescale $(\gamma \sim v_A/R)$. However, for a cold beam with a smaller degree of field reversal, or with aspect ratio near unity, so that $(T/E)(R/a) \ll 1$, the growth rate is exponentially smaller.

For a rigid rotor distribution function, an energy expression similar to that of Lovelace (described above) but treating the beam contribution by kinetic theory is derived. The frequency is given by

$$\omega = \pm \left[(\delta W - i\mathcal{R})/K \right]^{1/2}. \tag{14}$$

where δW is the nonresonant energy term, K is the kinetic energy term, and $\mathcal{R}$ is the resonant contribution; here,

$$\delta W = \delta W_p + (e^2\bar{\Omega}^2/2c^2) \int d^3x |\delta\psi|^2 \int d^3v f_0' + S.$$

$$S \sim -\frac{e^2 l\bar{\Omega}}{4\pi m^2 c^2} \int dp_\theta dH A(p_\theta,H) f_0' \, \mathcal{P} \int d\beta \frac{P(\beta)}{\beta + l\Omega}. \tag{15}$$

$$\mathcal{R} \sim \frac{e^2 l\bar{\Omega}}{4m^2 c^2} \int dp_\theta dH A(p_\theta,H) f_0' P(-l\Omega).$$

$A(p_\theta,H)$ is the four dimensional phase space volume accessible to a particle with energy H and canonical momentum p_θ. $P(\beta)$ is the power spectrum of betatron oscillations, and $\mathcal{P}$ denotes a principal value. For small beam density, $\mathcal{L}$ is negligible. When $\delta W < 0$, the mode is a hydromagnetically unstable mode of the background plasma modified by the presence of the beam, and $\mathcal{R}$ affects only the real part of the frequency to lowest order. When $\delta W > 0$ and $\mathcal{R} \neq 0$, resonant instability is present and the degeneracy of ideal MHD, $\omega = \pm(\delta W/K)^{1/2}$, is split. Alternatively,

$$|\omega|^2 + \delta W + \omega_r \mathcal{R}/\gamma = 0, \tag{16}$$

where $\omega_r = \text{Re}(\omega)$, $\gamma = \text{Im}(\omega)$. Thus for modes with $\delta W > 0$ and $f_0' = \partial f_\theta/\partial H < 0$, $\omega_r l\bar{\Omega}/\gamma$ must be positive, so that modes with phase velocity parallel to the beam velocity are unstable. Note that the stability criterion is not obtained by minimizing the energy with respect to ξ, and that since instability exists whenever $\mathcal{R} \neq 0$ this implies the absence of complete finite Larmor radius stabilization.

While theories which neglect betatron resonances and similar kinetic effects predict finite Larmor radius stabilization, Tasso has pointed out that finite Larmor radii cannot influence stability.[29] The resolution lies in the observation that the growthrates associated with resonant instability can be exponentially small in comparison with MHD growthrates. This point has also been made by Seyler and Freidberg.[30] Finally, nonlinear terms in the equation of betatron oscillatory motion change the power spectrum $P(\beta)$ from a sum of delta functions at linear combinations of the radial and axial betatron frequencies to a set of broadened peaks; this effect is important only when the width of $P(\beta)$ is very large or the beam temperature very small.

As a specific example, Finn and Sudan treat the kink mode of the field-reversed bicycle tire ion ring system in the straight beam limit; the trial function is given by $\xi = \xi_0 \hat{r} \exp(i\ell\theta - i\omega t)$. For low enough energy the orbits are purely harmonic, and assuming an exponential rigid rotor distribution, $\mathcal{R}$ is found to be:

$$\mathcal{R} = -\tfrac{1}{4}\pi^{3/2}(E/T)^{1/2}\xi_0^2 R \; \exp\left[\frac{E}{T}\left(1 - \frac{\ell_0^2}{\ell^2}\right)^2\right]. \tag{17}$$

where $\ell_0 = (R/a)(\zeta/\pi)^{1/2}$, and $T/E \sim \zeta/2\pi$. Since $\delta W_{MHD} \sim (\pi/4)\xi_0^2 B_0^2 R$, when $\ell \sim \ell_0$, $\mathcal{R}$ is largest and of the same order of magnitude as δW_{MHD}.

In the cold beam limit, the stability criterion $\omega_\beta^2 < \ell^2\Omega^2$ of Lovelace[16] is recovered. Ignoring resonances, δW is a strongly stabilizing influence when $\omega_\beta^2 < \ell^2\Omega^2$. When resonances are included, the analysis reveals that if $(R/a)(T/E) \sim (\zeta/2\pi)(R/a) \ll 1$, resonant modes with $\ell^2 > \ell_0^2$ have growth rates exponentially smaller than hydromagnetic (compare δW_{MHD}). Here, ζ is the field reversal on axis. However, for stronger rings with $(R/a)(T/E) \sim 1$, all modes have growth rates typical of hydromagnetic instability, with $\gamma \sim v_A/a$. In particular, without betatron resonances the stability criterion is $(R/a)^2\zeta/\pi < 1$, but with resonances included the condition for an exponentially small growth rate is $(R/a)^2\zeta/\pi \ll 1 - (T/E)^{1/2}$. For $\zeta = 1$ ($T/E = 1/2\pi$), the criteria become $R/a < 1.77$ and $R/a \ll 1.37$ respectively, and hence inclusion of the betatron resonance instability mechanism makes the kink mode stability criterion significantly harder to satisfy. A toroidal magnetic field is found to stabilize these modes either completely or by reducing their growth rates; however, such a toroidal field is not presently incorporated into our simulation program.

III. HYBRID SIMULATION MODEL

The simulation model employed in these studies, and its implementation into the RINGHYBRID code, have been described in detail elsewhere.[22] Here, we briefly describe the set of equations solved by the program, the assumptions made, and the code's limitations.

RINGHYBRID uses particle-in-cell simulation techniques to advance a set of finite-size "superparticle" clouds along their equilibrium orbits. The equilibrium field has components B_r, B_z which are consistent with the zero order azimuthal "beam" (energetic component) current $J_{b\theta}$ and charge density n_{qb}. This self-consistency is arrived at by solving Ampere's and Faraday's laws (without displacement current) on the computational mesh using $J_{b\theta}$ accumulated from the particles:

$$c\nabla\times\nabla\times(A_\theta\hat{\theta}) = (4\pi J_{b\theta} - \sigma^0\partial A_\theta/\partial t)\hat{\theta}. \tag{18}$$

where σ^0 is a constant; the effect of this term is to damp collective oscillations from the system.[23] Particles are injected over a number of steps into a field which is initially that of a solenoid plus two arbitrarily-located and –driven axisymmetric d.c. coils. The self-field thus builds up gradually. Plasma electron return currents are explicitly excluded at this point; this stage of the calculation is most properly thought of as an artifice aimed at generating a suitable equilibrium for the stability study, rather than as a detailed model of ring buildup in an actual experiment. The formation of equilibria by injection of simulation particles has been described in greater detail elsewhere.[23]

In addition to the hot-ion component, a cold, uniform background of ions (i) and a complement of cold electrons (e), of density such that charge neutrality obtains, are described by fluid equations. While these latter components have no zero order motion, their first-order response is of critical importance. Collisions between background electrons and ions are modeled by a scalar collision frequency ν_{ei}. Electron inertia and the displacement current are neglected; quasineutrality and low frequencies justify neglect of the longitudinal displacement current (as well as the transverse component, already neglected in the Darwin approximation). Since we do not solve Poisson's equation, no conflict with the charge continuity equation arises.

A field or current quantity $\underline{G}$ is represented by:

$$\underline{G}(r,\theta,z,t) = \underline{G}^0(r,z,t) + \underline{\delta G}\exp(i\ell\theta), \tag{19}$$

where θ is defined relative to the +x axis. Among the equilibrium quantities, only B_r^0, B_z^0, and n_{qb}^0 are used in the simulations, though $J_{b\theta}^0$ is needed to obtain the equilibrium. All first order fields and

currents are employed, and so $\delta E, \delta B$, and δJ require 18 arrays (since the perturbations are complex).

Particles are circular ring of finite cross-section, to zero order. To first order they are noncircular, each point p on the zero order particle being displaced to a point p' on the perturbed particle:

$$p' = p + \varepsilon \exp(i\ell\varphi). \qquad (20)$$

Here φ is defined relative to a "reference point" r on the particle; r moves with the zero order motion in r, θ, and z and is instantaneously located at an angle α with respect to the +x axis, so that $\theta = \alpha + \varphi$. We need only follow the motion at the perturbed reference point r', since ε contains the amplitude and phase information for displacements at all p'. Note that ε_θ may be nonzero, indicating a periodic bunching of the points comprising one simulation superparticle.

The first order simulation begins by advancing the "beam" particles along their equilibrium orbits, yielding $r(t)$, $\dot{r}(t)$, and $B(r(t))$; spatial derivatives of the last are obtained using using the derivatives of the zero order particle-mesh interpolation function. For each particle,

$$\ddot{\varepsilon} = (q/m)\{\delta E + \dot{r}\times[\delta B + (\varepsilon \cdot \nabla)B] + \dot{\varepsilon}\times B\}. \qquad (21)$$

Also using the particle-mesh interpolant and its derivatives, expressions for the components of δJ are evaluated for each particle in turn; these are too complicated to reproduce here.

The plasma model equations are:

$$0 = -n_e e(\delta E + \delta v_e \times B/c) - n_e m_e \nu_{ei}(\delta v_e - \delta v_i)$$
$$n_i m_i \partial \delta v_i / \partial t = n_i Z e(\delta E + \delta v_i \times B/c) - n_e m_e \nu_{ei}(\delta v_i - \delta v_e)$$
$$n_e = Z n_i + n_b \qquad (n_i = \text{constant}) \qquad (22)$$
$$c\nabla\times\delta B = 4\pi(\delta J_e + \delta J_i + \delta J_b)$$
$$c\nabla\times\delta E = -\partial\delta B/\partial t.$$

A dimensionless resistivity $\eta = m_e \nu_{ei}/Z n_i e^2$ is incorporated; however, we have not studied its effect upon ring stability. This set of equations, with δJ_b treated as a source term, is solved using centered differencing in time. Then, a corrector iteration is performed for the purpose of obtaining an improved δJ_b.

A generated equilibrium was allowed to "settle down" with the resistive relaxation turned on for (typically) 950 timesteps, at which time the equilibrium fields would be "frozen". At timestep 1000, the timestep counter would be reset to zero, a perturbation (for example, with $\ell = 1$) excited and the linearized simulation performed until the desired number of timesteps had been completed. Since a copy of the

state of the system would normally be saved immediately before the timestep counter was set to zero, this latter perturbation could be set by the user to have any value of l, any symmetry (i.e. axial mode symmetry, radial mode symmetry, random excitation, etc.), and any value of the background plasma density, since the last does not come into the equilibrium itself when the background is assumed pressureless, as in RINGHYBRID. Thus, a "family" of runs would be made starting from the same equilibrium state.

Our initial efforts in the study of field reversed ion rings using the RINGHYBRID code were frustrated by the appearance of rapid single-particle instability, arising from the exponential separation of the perturbed and unperturbed orbits with time.[23] During the course of experimentation with the code, we discovered one particular field-reversed equilibrium (a moderately thick ring) for which the rate of single-particle growth was sufficiently low that collective behavior was not unduly masked. That such configurations exist might be conjectured on the basis of work by others,[24] which showed a strong model-dependence of the ion ring's stochastic properties. In the following section we describe this equilibrium, and our simulation results regarding its low-frequency stability.

Addition of spatial filtering did not affect results, nor did use of metallic endwall boundary conditions, in the KR-series of runs.

IV. STABILITY OF A MODERATELY THICK ION RING

The runs to be described model a moderately thick ring which did not suffer unduly from single-particle instabilities. The equilibrium (run "KR") was formed by the injection of 2400 superparticles, each with charge $W = .04$, into a simulation region represented on a 48 cell (r) by 48 cell (z) grid. The actual region of injection was the interior of an oval, contained within $r = 10$ and $r = 20$, $z = 18$ and $z = 30$. Parameters were such that the (external field) ion cyclotron period was 40 timesteps, i.e. $\omega_{ci}\Delta t = .157$. The equilibrium field was frozen at timestep 950, and the perturbation initiated at timestep 1000. A number of hybrid-model simulations were carried out using various values of l and two values of the background density ρ_i. The equilibrium configuration is illustrated in fig. 2(a-d), which shows (respectively) contours of $J_{b\theta}^0$ in the r-z plane, field lines (equally spaced contours of $\nabla\psi$, where $\psi = rA_\theta$), particle locations, and contours of the mean angular velocity at each point in space. It is evident from the figure that the ring is moderately thick, fully field-reversed, and well removed from the radial vessel wall. More detailed diagnostics show that the ring contains only confined particles, and that it is <u>not</u> rotating "rigidly" — in fact the mean angular velocity varies by about

−14−

60% over the ring, being greatest at the regions of small radius. The orbit of a typical particle in this equilibrium is depicted in fig. 3; in a), the view is down the z-axis, while in b), the trajectory is shown in (r,z) space.

Parameters for this equilibrium are as follows. The wall lies at $r_w = 48$(cells), and the system is periodic in z with a periodicity length $L = 48$. This is long enough that we expect little interaction between the "neighboring rings" of the nearby periods. Growth times are of order of magnitude a/v_A, while Alfven transit times to the next period are larger by a factor L/a. The major radius of the ring was $R = 18$, with r.m.s. halfwidths $a_r = 2.9$, $a_z = 3.8$ (for purposes of the stability calculation, these are underestimates, and values taken from the separation between peaks of $|J_{b\theta}^1|$ when a perturbation is initialized are ~4.5 and ~5.0 respectively, leading to an aspect ratio of order 4:1). Although the external-field ion cyclotron period was $\tau_{ci} = 40$ steps, due to the self-field effect the mean gyration period τ_g was 79 steps ($\Omega\Delta t = .08$). Noting that the ratio of thermal to directed energy $T/E \sim \zeta/2\pi \sim 0.27$, we estimate $|v_r|/|v_\theta| \gtrsim 1/2$; this is confirmed by observing typical particle orbits which have $|v_\theta| \sim 1.5$, $|v_r| \sim 0.8$ near the center of the ring. Also, $\zeta_{max} \approx 1.7$, and $\zeta_{axis} \approx 1.35$. An effective self-field betatron frequency was calculated, as described in the above dicussion of Lovelace's theory, yielding an axial betatron frequency of $\omega_{\beta z} \approx .2$. Folding in the effect of the gyratory motion, the radial betatron frequency is found to be approximately $\omega_{\beta r} \approx .26$. These are only crude estimates, and in reality there are considerable spreads (of perhaps 20%) to these frequencies; by looking at a few representative particle orbits these numbers were checked and found to be reasonable estimates.

Thus, on the basis of the analytic theories of Lovelace and of Sudan and Rosenbluth described above, we have the sufficient condition for stability of axial kink modes $\ell\Omega > \omega_{\beta z}$, and hence would expect the $\ell = 1$ and 2 axial kink modes to (probably) be unstable, while the $\ell \gtrsim 3$ modes would be stable. For the radial modes, we have (for $\ell > 1$) $\ell\Omega > \omega_{\beta r}$ sufficient for stability, and thus expect $\ell = 2,3$ radial modes to be unstable, with $\ell \gtrsim 4$ modes stable. Furthermore, for the radial $\ell = 1$ MHD precession, we expect stability since there is no external field gradient and there is a stabilizing image current-induced equilibrium field gradient. As shown by Finn and Sudan (discussed above), the effects of particle betaton resonances ($\ell\Omega \sim \omega_\beta$) would be expected to alter these predictions somewhat. As will be seen, our simulations show the gross stability properties of the system to be in close agreement with theoretical predictions neglecting the resonant effects, and also show much weaker instability in some cases which may possibly be attributed to betatron resonance instability.

As an aside, note that simulation variables are related to a specific set of physical (CGS,MKS) variables only when Δr and Δt are specified in physical units (in code units they are both unity).[22] Thus, there is a two-parameter family of physical situations associated with each simulation run. To give a specific example, if for the present series of runs we associate $\Delta r \to 0.5$cm., $\Delta t \to 1.0$ns., then the physical system has: $R = 9$cm., $r_w = 24$cm., $B_{ext} = 16.4$kG., $v_\theta = 7.2 \times 10^8$cm/s., $n_b = 1.4 \times 10^{14}$cm^{-3}, $I = 320$kA., $J = 1.6 \times 10^4$A/cm^2 (typical), and the ring is made up of 1.6×10^{17} protons, each with a (typical) energy of 0.5MeV. Of course, by varying the assumptions concerning Δr and Δt, a ring with (say) $R = 36$cm. would be represented by the same simulation run. To summarize, any number of physical scenarios are represented by one run; it is the set of dimensionless parameters (such as ζ_{max}, ζ_{axis}, a_r/R, etc.) which are of fundamental importance.

For most of the runs in this series, the background plasma density (in dimensionless units) was set to $\rho_i = 4$. This corresponds to a density ratio $\rho_b(\text{max})/\rho_i = .018$, and a velocity ratio $v_0/v_A = 18.5$.

The code was allowed to run without calculating first order currents and fields, so that the $\underline{\varepsilon}_k$ should have a chance to grow due to the presence of single-particle instability. Figure 4 shows the components of $|<\underline{\varepsilon}>|$ as functions of time between steps 2000 and 4000; weak "stochastic" growth is evident, with $\gamma/|\omega_{ci}| \sim .015$. Thus, we are unable to diagnose weak collective instability with growth rates less than about .015.

$l = 1$ Results

The first hybrid-model run in the series was "KRAA"; for this run an $l = 1$ perturbation having both radial and axial components was initiated at "timestep zero." This initialization is depicted in fig. 5, part a). The top half of the figure shows eight "tracer" particles at timestep zero, viewing the system along the z axis. The initial "rigid" off-center displacement of the ring is evident. The left lower section of the figure contains the same information, but the ring has been "unwrapped", so that θ ranges from 0 to 360° along the ordinate and r ranges from 0 to 48 along the abscissa. Finally, the right lower section shows an unwrapped ring viewed looking down the x-axis; the axial perturbation (tilt) is evident here — it has been initialized 90° out of phase with the radial excitation. Note that the (strictly infinitesimal) perturbation was initialized with unit magnitude in the code — since the system is linearized the numerical magnitude of the initial perturbation is irrelevant. For the creation of these "snapshots" the $\underline{\varepsilon}_k$'s were multiplied by a suitable constant to

render them visible, before adding them to the zero order location of each point on the tracer particle k.

Figure 5, part b) shows the same quantities at timestep 1000 (the end of the run). Because (as will be seen) only the axial mode is unstable, only the lower-right plot in the figure shows coherent structure. Most of the eight tracer particles are displaced approximately in phase with each other in the axial direction. Here, the ξ_k's have been divided by $6\mathrm{X}10^2$, as the axial mode has grown by almost three decades.

This growth can be seen more clearly in fig. 6, which shows the components of $|<\underline{\xi}>|$ as functions of time, between timesteps 0 and 1000. It is evident that the axial kink mode is unstable, with a growth rate of $\gamma' = \gamma/|\omega_{ci}| \approx .053$. The mode is clearly hydrodynamic in character, as $\gamma_{MHD}/\omega_{ci} \sim v_A/a\omega_{ci} \sim 0.1$ is a reasonable order-of-magnitude estimate of the growth rate. The mean radial displacement (and the mean azimuthal displacement, to which it is coupled by the geometry of the system) does not grow with time. That is, this ring is stable to the $\ell = 1$ radial mode ("MHD precession"). Since no external field gradient was applied, the stability of this mode is to be expected.

Examination of the phase behavior of the mean $\underline{\xi}$, fig. 7, confirms these findings. The quantities $<\varphi_r>$ and $<\varphi_\theta>$ show no single clear structure (the structure in $<\varphi_\theta>$ can be termed a "bump on the ring" effect, that is, a stable perturbation traveling with the layer, since its phase advances at approximately the gyration frequency). In contrast, $<\varphi_z>$ shows a slow, steady advancing of phase (after the unstable mode has come up out of the noise), with a real frequency $\omega' = \omega/|\omega_{ci}| = .0076$. Clearly this is much smaller than unity, and so assumptions of a low-frequency mode are well justified. Also note that the growthrate $\gamma \sim 0.008$ is greater than the inverse of the Alfven transit time to the walls, $v_A/L \leq 0.003$, so that endwall effects can be expected to be unimportant, and the mode is "local", in this sense.

The structure of this unstable mode has been diagnosed in considerable detail. In fig. 8 are depicted the mean first order displacements of the ring particles as a function of r-z position, at the end of the run. These were obtained by summing the ξ_k of all particles in each grid cell (using the particle-mesh interpolatory spline), then dividing by the number of particles in the cell. In the two boxes at the left of the figure the two-dimensional vector $(<\xi_r>,<\xi_z>)$ is drawn as an arrow with its center over that of the corresponding grid cell and its length proportional to that of $\xi_{r,z}$. The upper figure depicts the displacement at $\theta = 0°$, while the lower figure depicts that at $90°/\ell$. Examination of the latter reveals the mode to be nearly a rigid "tilt" about a point somewhere between the edge of the ring and the z axis. The orientation of this tilt, with a maximum positive displacement at $\theta = 90°$, is also evident in fig. 7,

which shows the "mean phase" $\langle\varphi_z\rangle$ at the end of the run to be roughly
90°. The two boxes at the right of fig. 8 depict zonally averaged
azimuthal displacements $\langle\varepsilon_\theta\rangle$, with an up-arrow indicating a positive
displacement. These arrows are drawn to the same scale as those of the
corresponding frame on the left. At 90° there is almost no azimuthal
displacement, but at 0° the principal displacement is azimuthal. Note
the left-right antisymmetry.

Another diagnostic of the mode structure is presented in fig. 9,
wherein "slices" through the middle of the ring were taken. On the
left, the dependence of $\underline{\varepsilon}$ upon r at $z = z_{mid}$ is shown. The uppermost
frame depicts $\langle\varepsilon_r\rangle$ at $\theta = 0°$ (solid) and 90° (dashed). The middle and
lower frames similarly show $\langle\varepsilon_\theta\rangle$ and $\langle\varepsilon_z\rangle$. Note that the lowest curve
on the left embodies the nearly-rigid "tilt" structure. On the right,
$\langle\underline{\varepsilon}\rangle$ as a function of z at $r = 17.5$ (approximately the mean radius of the
particles) is shown, again with r,θ,z components from top to bottom.

Similar diagnostics for the first order beam current appear as
fig. 10 and fig. 11. They reveal it to have a large positive component
at the right of the ring, and a similar but negative component on the
left. A smaller positive $J^1_{b_z}$ at $\theta = 0°$ can also be noted.

Figure 12 depicts the first-order magnetic field at the end of the
run. Note how field lines encircle the peaks of positive and negative
azimuthal beam current (the arrows in the lower figures would be three
times as long as those of the upper figures, were they drawn to the same
scale). Similar diagnostics for the first order electric field reveal
its principal component to be azimuthal, left-right antisymmetric, and
of roughly equal magnitude but opposite sign at $\theta = 0°$ and 90°.

The plasma ion current is smaller in magnitude than the beam
current; its spatial pattern is entirely different, as seen in fig. 13.
Finally, fig. 14 depicts the total current obtained as the curl of $\underline{B}^1$.
Its dominant azimuthal component is smaller than, but similar in pattern
to, that of the beam current.

$l = 2$ Results
_____

The second run to be considered is "KRBA", which was given an $l = 2$
excitation at timestep zero. The evolution of the components of the
mean amplitude $|\langle\underline{\varepsilon}\rangle|$ is shown in fig. 15. As anticipated, both axial
and radial $l = 2$ modes are unstable. Note in the figure that the radial
and azimuthal components grow at the same rate (as they must),
$\gamma'_r = .091$, while the axial component $|\langle\varepsilon_z\rangle|$ grows at a slightly faster
rate, $\gamma'_z = .098$ (the difference can be seen if a parallel-line ruler is
applied to the figure). Note that these growth rates are higher than
that of the $l = 1$ axial mode.

That the radial and axial modes have different frequencies is more
clearly evident in fig. 16, which shows the temporal evolution of the
phases of the mean displacement components. Radial and azimuthal phases
advance at a very low frequency $\omega_r' = .024$, while the axial phase
advances at $\omega_a' = .133$. Note that these frequencies were calculated from
the period associated with motion of the displacement through 180°,
since in the laboratory frame of reference an $l = 2$ displacement would
appear identical under a rotation through 180°. The period for each
point of the wave pattern to move through a full circle would be twice
as long, so the apparent angular velocity of the mode is half the quoted
frequency.

The same run with only an initial radial perturbation was made, for
purposes of diagnosing the mode structure; it was called NNHA.
Snapshots of the "tracer" particles at a time halfway through the run,
and at the end of the run, are depicted in fig. 17. Note that the
perturbations to the particle shapes are drawn to different scales at
the two times. The points comprising the simulation particles at small
radius exhibit strong azimuthal bunching. Mean displacements $<\underline{c}>$ at the
end of the run are depicted in fig. 18. The upper frames are at $\theta = 0°$;
the lower are at 45°, and their arrows would be half as big as drawn
were they to scale. From fig. 16 we see an expected peak displacement
at $\theta = 80°$ (and also at -10°, 170°, and 260°). Note how nearly rigid
this mode is as a function of r and z. The first order magnetic field
pattern for this run is shown in fig. 19; again, field lines encircle
the beam current.

The same run with only an initial axial perturbation was also made
(NNIA). Snapshots of the "tracers" at the end of the run are shown in
fig. 20. The upper right of the figure is a three-dimensional
representation of the perturbed ring, while the lower right shows
"slices" at various values of θ. Mean displacements at the end of the
run are shown in figs. 21,22; no rigid structure is discernable. The
peak mean axial displacement, from fig. 16, is at about $\theta = 120°$ and
300°, with negative peaks at 30° and 210°. Thus, neither snapshot
depicts the mode structure at the θ of maximum displacement, and so the
mode may in fact have a more rigid structure than that suggested by the
figures.

$l = 3$ Results

Two runs with initial $l = 3$ perturbations were carried out; these
were KRCA and KRIA. In the former, both radial and axial components
were excited, while in the latter only the axial component was excited.
The reason the latter run was made is that in the former run, the

rapidly growing unstable radial mode "corrupted" the stable axial mode
after about 300 timesteps, and the axial mode began growing with the
same growth rate as the radial mode. This is due to a weak (numerically
induced) coupling of the radial and axial modes, which arises from small
left-right assymmetries in the system (due to weakly stochastic orbits,
for example). Since it was desirable to verify the stability of the
$l = 3$ axial mode over a longer period of time, the latter run (KRIA) was
made, and results from this run are shown here. The growth of the axial
mode in KRCA was clearly nonphysical, as it was locked in phase to that
of the radial mode, and disappeared when the radial mode was not
excited.

In fig. 23 the components of $|<\underline{\varepsilon}>|$ are shown as functions of time.
The radial mode, which was not initially excited, grows up out of noise
anyhow (due to the weak assymmetry-induced coupling with the axial
mode). Its growth rate is the largest of any mode for this equilibrium,
with $\gamma' = .12$. The mean axial displacement $|<\varepsilon_z>|$ behaves identically
to that observed in KRCA for 300 timesteps. However, in contrast to
that run it shows stability (or at worst, very slow growth) out to
approximately timestep 800, when it too appears to be "corrupted" by the
many-decades-larger unstable radial mode, in much the same way as it was
in KRCA at an earlier time. On the basis of the time-history of $|<\varepsilon_z>|$
between steps 0 and 800, an upper limit to the growth rate of the $l = 3$
axial mode can be established at $\gamma' < .02$. The axial mode may in fact
be stable, and the weak growth an artifact of the single-particle growth
mechanism; or it may be very weakly unstable. A possible mechanism for
instability is the betatron resonance effect of Finn and Sudan
(described above). Since $3\Omega \sim .24$ and some of the $\omega_{\beta k}$'s can be expected
to fall near this value, a betatron resonance instability is at least
plausible in this case.

The mean phases of the $l = 3$ run KRIA are shown in fig. 24 as
functions of time. The real frequency of the radial mode is $\omega' = .165$.
The axial mode contains a real frequency component at $\omega' = .25$; that
this component is visible at all is a suggestion that a weak instability
(quite different in character from the "classical" kink mode instability
in the radial direction) is present. Numerical coupling to the radial
mode can be ruled out since the frequencies of the radial and axial
modes differ. Finally, we note that the phase of the axial mode
advances in the forward ($+\theta$) direction, as necessary for a
betatron-resonance instability, and that Finn and Sudan's l_0, the value
of l for which the resonant term $\mathcal{R}$ is maximal, is of order 3 for this
equilibrium.

Mean $\underline{\varepsilon}$'s as functions of r and z are shown in fig. 25. The peak
positive radial displacement occurs at $\theta = 20°$ (and also $140°$ and $260°$),
while the plots are at $0°$ and $30°$. Note the concentration of $<\varepsilon_r>$ near
$z = z_{mid}$.

$l = 4$ Results

Initial radial and axial perturbations were applied to the ring in run KREA. In contrast with the run described above, no component of $|<\underline{\varepsilon}>|$ in fig. 26 shows clear exponential growth. Instead, the radial and azimuthal components show "ragged" growth at $\gamma' = .037$. (Recall that, for $l = 1,2,3$, as l was increased the growth rate of the radial mode also increased, and growth was purely exponential.) The axial component does not show such a rapid increase in amplitude, and may be stable; an upper limit to its growth rate is $\gamma' < .018$. Mean phases for this run are shown in fig. 27. It is hard to determine any real frequencies here, but the radial displacement appears to have a component at $\omega' = .3$

In an attempt to determine how much of this growth could be directly attributed to the single-particle stochastic growth mechanism, another run, KRFA, was made. In this run, the first-order current accumulation and fieldsolving were deactivated, so that $E^1 = B^1 = 0$, and the separation of neighboring orbits in the equilibrium field would be the only possible growth mechanism. Figure 28 shows the components of $|<\underline{\varepsilon}>|$ as functions of time for this ring (phases, not shown, have no apparent structure). The radial and axial growth rates due to the single-particle mechanism appear to be between .015 and .018. In fact, the axial displacement $|<\varepsilon_z>|$ looks much the same as it did in the full hybrid model run KREA. However, the radial and azimuthal displacements in KREA appear to grow somewhat more rapidly than those in KRFA; this suggests that there may in fact be a weak instability of the $l = 4$ radial mode. Again, a possible explanation for this is that $4\Omega \sim .32$ may not be greater than all the $\omega_{\beta k}$'s, since there is a considerable spread to these quantities and a nominal value for $\omega_{\beta r}$ is .26. However, this growth may possibly also be nonphysical, and due to the single-particle mechanism. The average $|<\varepsilon_{r,\theta}>|$ may be larger when collective effects are included merely because a weak phase-correlation of other particles with the displacements of the most-unstable particles has been introduced. The lack of structure to the phases further suggests the absence of a true unstable collective mode.

$l = 5$ Results

Run KRGA was an $l = 5$ study of the same equilibrium, involving initial axial and radial excitations. Time histories of the components of $|<\underline{\varepsilon}>|$ for this run are shown in fig. 29. An upper limit to the radial mode growth rate is $\gamma' < .022$, while for the axial mode an upper

limit is $\gamma' < .029$. Both of these growth rates are roughly consistent with the stochastic growth mechanism (with the average $\underline{c}$'s being modified somewhat by interparticle couplings). This is confirmed by the phases shown in fig. 30, which show no evident structure, as expected for single-particle type growth.

$l = 1$, Denser Plasma Results

Run KRDA, and its continuation KRDB, model a system wherein the background plasma density was made larger by a factor of four than it was in the above runs; $\rho_b(max)/\rho_1 = .0044$. Figure 31 shows the time histories of the components of $|<\underline{c}>|$ between timesteps 0 and 2000 (note that this run was twice as long as the others so that the slower growth could be measured). Mean phases are shown in fig. 32. As in the less-dense-background run KRAA, the radial mode (involving $<c_r>$ and $<c_\theta>$) is observed to be stable — note that the mean phases of these components show no structure. Furthermore, the axial mode is again unstable, with $\gamma' = .028$ and $\omega' = .002$. The growth rate is approximately half that observed in the run where ρ_1 was 1/4 as large, while the real frequency is about 1/3 as large. Such a scaling of the growth rate with the inverse square root of the background density (i.e. with the Alfven speed in the background plasma) is suggested by theory as described in section IIA.[16]

A summary of the results for the runs described so far (KR-series) is presented in Table 1.

Runs With Thinner Rings

For a series of thinner ion rings, we have observed large growth rates and unstable modes up through $l = 7$. A summary of the results for this series of runs (KP-series) is presented in Table II. In this series, as well as in some other thin ring runs, there is an instabiltiy of the $l = 1$ azimuthal and radial motion which corresponds to a "bunching" of the ring. This latter instability may be an artifact of the small number of grid cells over which particles move in the thin ring runs, or it may be a physical instability similar in character to "negative mass" instability.

V. SUMMARY AND CONCLUSIONS

We have found one particular equilibrium for a moderately thick, field reversed ion ring with aspect ratio of order 4:1 for which single-particle instability was not excessively rapid. For this ring, we have observed non-resonant kink mode behavior in good agreement with predictions based on the thin ring theories of Lovelace, and of Sudan and Rosenbluth. In addition, we observe additional instability which may correspond to the betatron resonance mechanism of Finn and Sudan, although because of the masking effect of single-particle modes it is difficult to make a conclusive identification.

Since the most dangerous modes of the moderately thick ion ring appear to be the nonresonant kink modes, some means of stabilizing these modes must be found. Studies by Finn suggest that a toroidal field would suffice to stabilize these instabilities; its strength might be well below the Kruskal-Shafranov value[31] (the resonant kink modes might also be stabilized by a toroidal field[28]). Stability of the $l = 1$ radial mode (MHD precession) in a uniform external field does not appear to be a problem if there is a wall at finite distance, since image currents in the wall provide a favorable field gradient. However, if the ring is contained within an external mirror field with a corresponding negative radial field gradient, the wall may have to be quite close to provide stabilization. Alternately, a favorable gradient might be provided by an external quadrupole field, but the introduction of zero-order nonaxisymmetry may introduce a host of other instabilities, such as single-particle resonance instabilities.[32,33] The higher azimuthal mode number nonresonant kink modes are stabilized by a larger inverse aspect ratio, which has the main effect of lowering the betatron frequency by making the effective potential well more shallow. There may well exist equilibria which are stable to these gross modes. Finally, we expect that low-frequency instabilities such as the ones herein described might efectively be stabilized by feedback techniques. Nonlinear studies must be performed to determine which modes are truly dangerous and which saturate in a benign manner (such as by thickening the ring slightly).

ACKNOWLEDGMENTS

REFERENCES

[1] R. N. Sudan and E. Ott, Phys. Rev. Lett. 33, 355 (1974).

[2] H. H. Fleischmann and T. Kammash, Nucl. Fusion 15, 1143 (1975).

[3] N. C. Christofilos, in Peaceful Uses of Atomic Energy (Proc. 2nd UN Conf. Geneva, 1958) 52, 279.

[4] G. A. Carlson, W. C. Condit, R. S. Devoto, J. H. Fink, J. D. Hansen, W. S. Neef, and A. C. Smith, Jr., Lawrence Livermore Laboratory Report no. UCRL-52467 (1978).

[5] M. N. Rosenbluth and M. N. Bussac, Nucl. Fusion 19, 478 (1979).

[6] A. G. Eskov et.al., Proc. 7th European Conf. on Controlled Fusion and Plasma Physics, Vol. I, p. 55 (lausanne, Switz., 1975)

[7] R. N. Sudan and P. Kaw, Phys. Rev. Lett. 47, 575 (1981); C. Litwin, R. N. Sudan, and A. D. Turnbull, Phys. Fluids 27, 2791 (1984).

[8] M. Gerver and R. N. Sudan, Phys. Fluids 22, 686 (1979).

[9] H. P. Furth, Phys. Fluids 8, 2020 (1965).

[10] R. V. Lovelace and R. N. Sudan, Phys. Fluids 15, 1862 (1972).

[11] H. L. Berk and R. N. Sudan, Plasma Phys. 6, 413 (1971).

[12] R. V. Lovelace, Phys. Fluids 22, 591 (1979).

[13] K. D. Marx, Phys. Fluids 11, 357 (1968).

[14] R. V. Lovelace, Phys. Fluids 21, 1389 (1978).

[15] J. L. Johnson, R. M. Kulsrud, and K. E. Weimer, Plasma Phys. 11, 463 (1969); L. Sparks and R. N. Sudan, Phys. Fluids 27, 626 (1984).

[16] R. V. Lovelace, Phys. Rev. Lett. 35, 162 (1975); Phys. Fluids 19, 723 (1975).

[17] R. N. Sudan and M. N. Rosenbluth, Phys. Rev. Lett. 36, 972 (1976); Phys. Fluids 22, 282 (1979).

[18] J. J. Bzura, T. J. Fessenden, H. H. Fleischmann, D. A. Phelps, A. C. Smith, and D. M. Woodall, Phys. Rev. Lett. 29, 256 (1972)

[19] B. Marder and H. Weitzner, Plasma Phys. 12, 435 (1970).

[20] D. V. Anderson, J. Killeen, and M. E. Rensink, Phys. Fluids 15, 351 (1972).

[21] J. M. Finn and L. Sparks, Cornell Univ. Laboratory of Plasma Studies Report no. 230 (1977).

[22] A. Friedman, R. N. Sudan, and J. Denavit, J. Comput. Phys 40, 1 (1981).

[23] A. Friedman, J. Denavit, and R. N. Sudan, J. Comput. Phys 44, 104 (1981).

[24] J. M. Finn and R. N. Sudan, Nucl. Fusion 22, 1443 (1982)

[25] E. P. Lee, Phys. Fluids 16, 1072 (1973).

[26] S. Humphries, Jr., Nucl. Fusion 17, 859 (1977).

[27] I. B. Bernstein, E. A. Frieman, M. D. Kruskal, and R. M. Kulsrud, Proc. Royal Soc. London A 244, 17 (1957).

[28] J. M. Finn and R. N. Sudan, Phys. Rev. Lett. 41, 695 (1978); Phys. Fluids 22, 1148 (1979).

[29] H. Tasso, in Plasma Physics and Controlled Nuclear Fusion Research (IAEA, Vienna, 1977) Vol. III, p. 371.

[30] C. E. Seyler and J. Freidberg, in Proceedings of the Annual Controlled Fusion Theory Conference, Gatlinburg, Tenn., 1978.

[31] J. M. Finn, Phys. Fluids 22, 1770 (1979).

[32] S. C. Luckhardt and H. H. Fleischmann, Cornell Univ. FRL Rept. No. 14 (1979).

[33] R. H. Cohen, D. V. Anderson, and C. B. Sharp, Phys. Rev. Lett. 41, 1304 (1978).

TABLE 1. Summary of results for moderately thick ion ring (series KR). Results for modes with growth rates less than about .04 are uncertain due to "single-particle" instability, while all others should be unaffected since the collective mode is dominant.

Run	Mode	γ'_{radial}	γ'_{axial}	ω'_{radial}	ω'_{axial}
KRAA	$l = 1$	~0	.053	–	.0076
KRBA	$l = 2$	.091	.098	.024	.133
KRCA,IA	$l = 3$	.12	~0	.165	–
KREA	$l = 4$	<.037	<.018	–	–
KRFA	$l = 4$, s.p.	.015	.018	–	–
KRGA	$l = 5$	<.022	<.029	–	–
KRDA,B	$l = 1$, $\rho = 16$	~0	.028	–	.002

("s.p." : single-particle run, $E^1 = B^1 = 0$)

TABLE II. Summary of results for thinner ion ring (series KP).

Run	Mode	γ'_{radial}	γ'_{axial}	ω'_{radial}	ω'_{axial}
KPAA	1	<.031	.063(s.m.)	.24	–
KPBA	2	.063	.095	.01	.02
KPCA	3	.205	.239	.053	.084
KPDA	4	.347	.381	.164	.229
KPGA	7	.469	.484(end)	.792	1.0(end)
			.337(beg)		.79(beg)

("s.m." : single particle mode)

FIGURE CAPTIONS

Fig. 1. Depiction of field reversed ion ring geometry.

Fig. 2. Clockwise from upper left: contours of $J_{b\theta}^0$ in r - z plane, fieldlines, contours of mean angular velocity, particle locations, for equilibrium run KR.

Fig. 3. Typical particle orbit: a) view down axis; b) path in r-z space.

Fig. 4. Amplitudes of components of mean displacement versus time for run KR, with $E^1 = B^1 = 0$. The slow exponential growth reflects the separation of intrinsically unstable orbits in the equilibrium field.

Fig. 5. Snapshots of tracer particles for run KRAA. (a) Timestep 0. (b) Timestep 1000.

Fig. 6. Mean amplitudes of radial, azimuthal, and axial components of particle displacements versus time for run KRAA ($l = 1$).

Fig. 7. Mean phases of radial, azimuthal, and axial components of particle displacements versus time for run KRAA ($l = 1$).

Fig. 8. Mean displacements of ring particles at end of $l = 1$ run versus r-z position (see text).

Fig. 9. Mean displacements of ring particles for $l = 1$ versus r and versus z (see text).

Fig. 10. First order beam current versus r-z position for $l = 1$.

Fig. 11. First order beam current versus r and versus z for $l = 1$.

Fig. 12. First order magnetic field versus r-z position for $l = 1$.

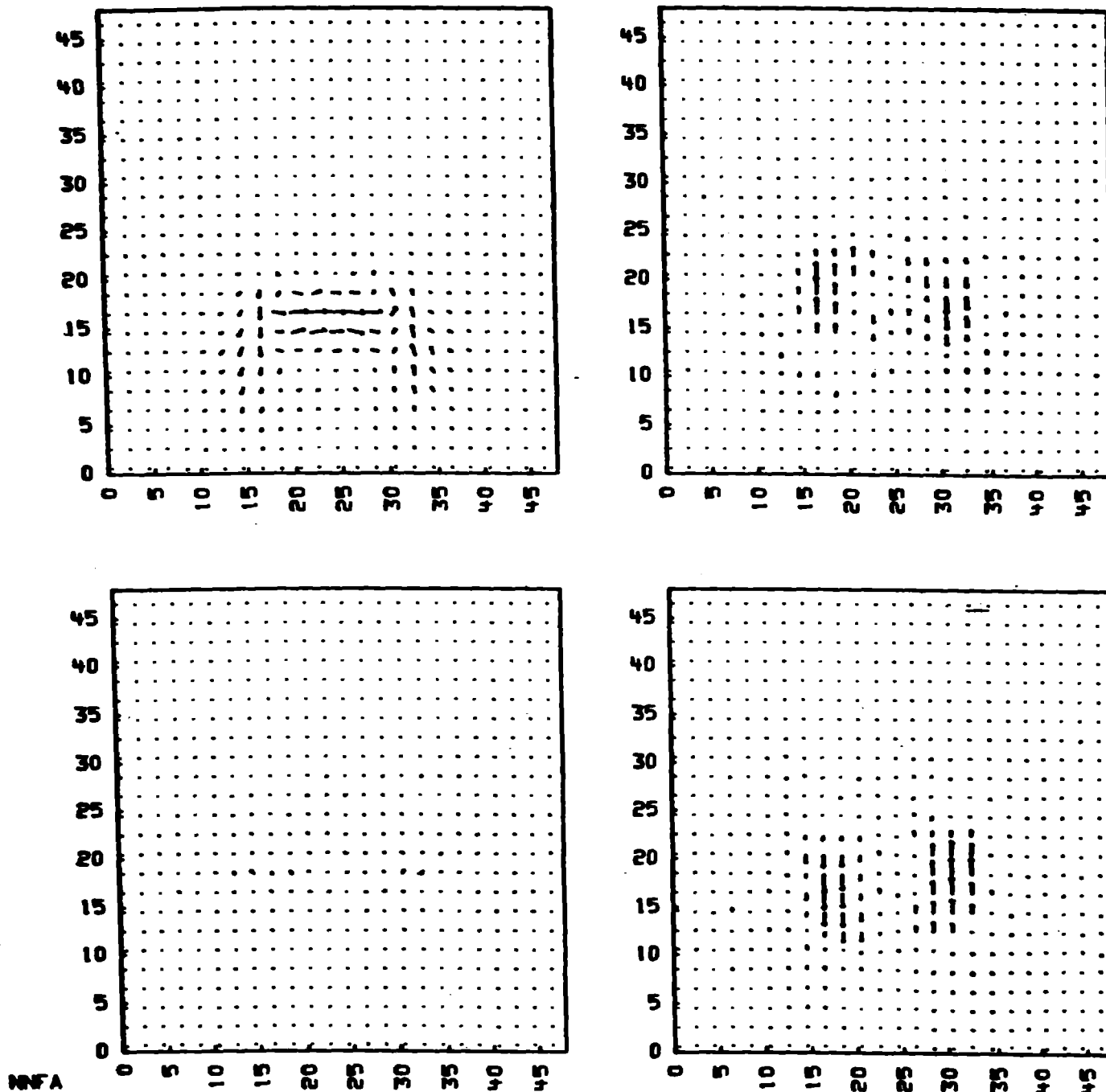Fig. 13. First order plasma ion current versus r-z position for $l = 1$.

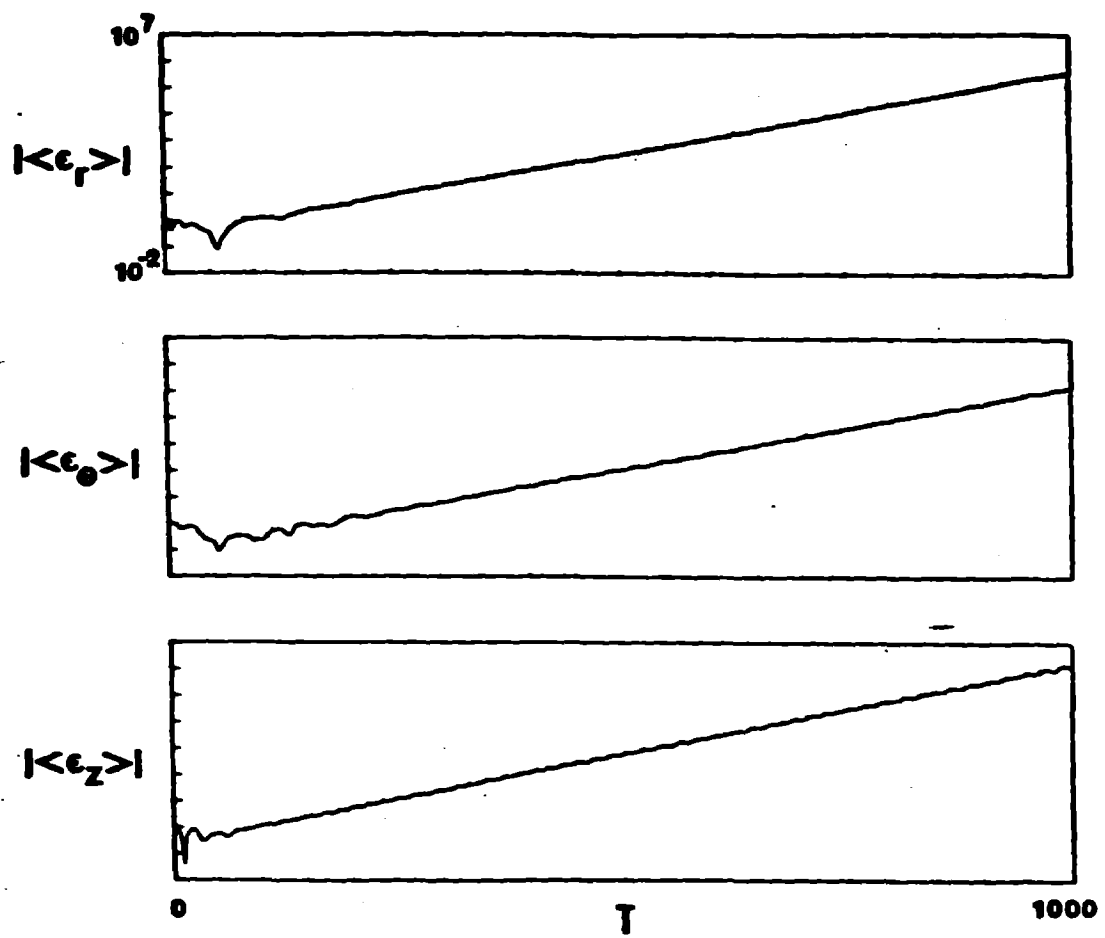Fig. 14. First order total current versus r-z position for $l = 1$.

Fig. 15. Mean amplitudes versus time for run KRBA ($l = 2$).

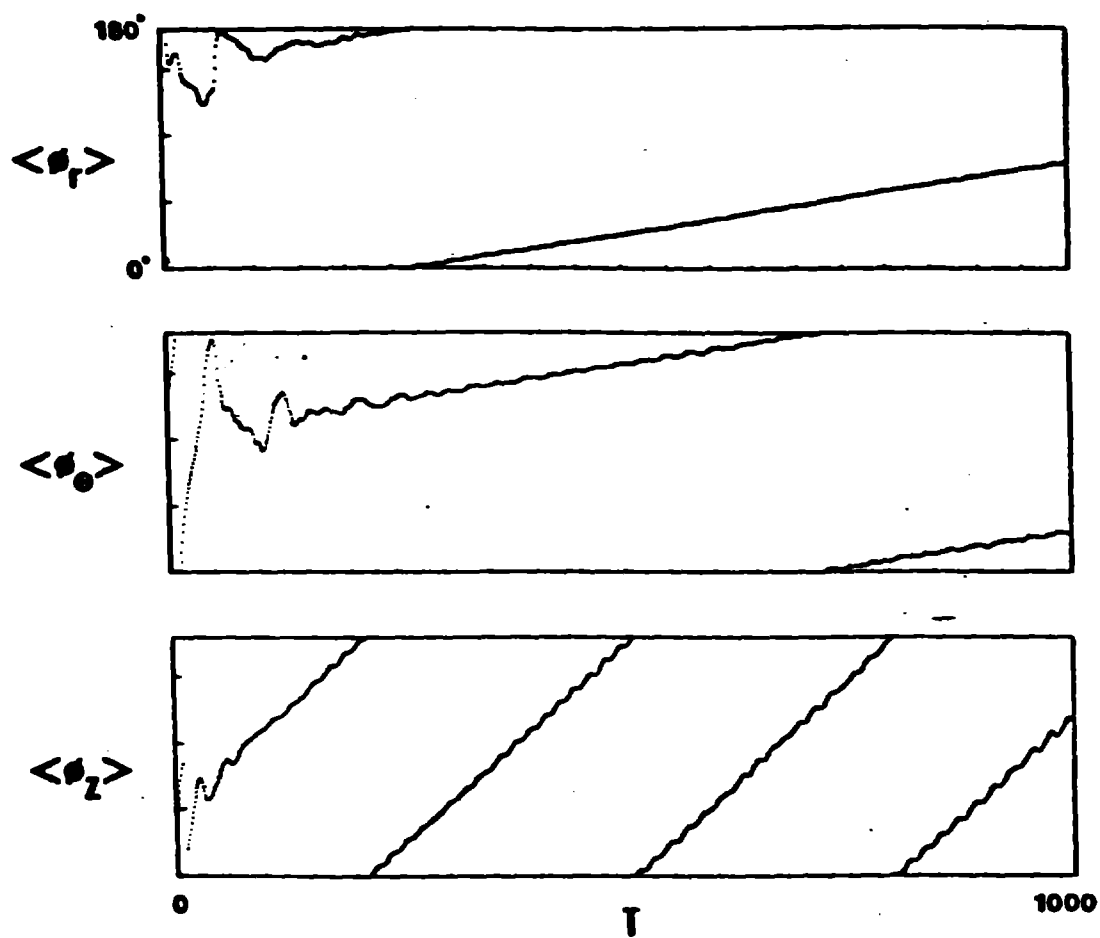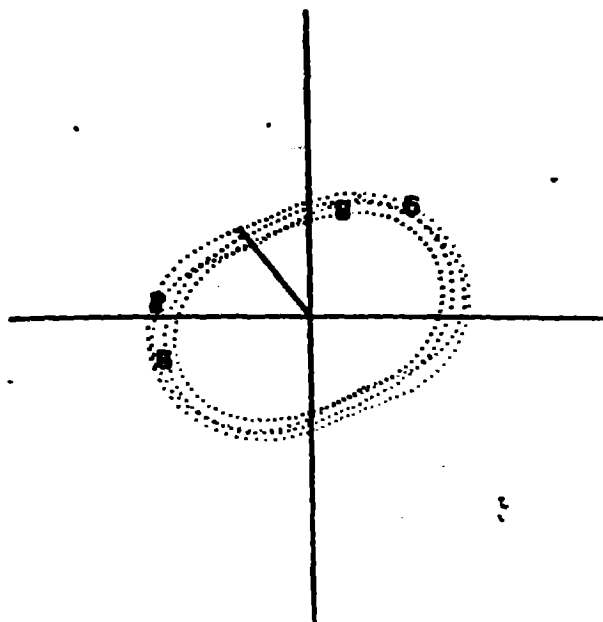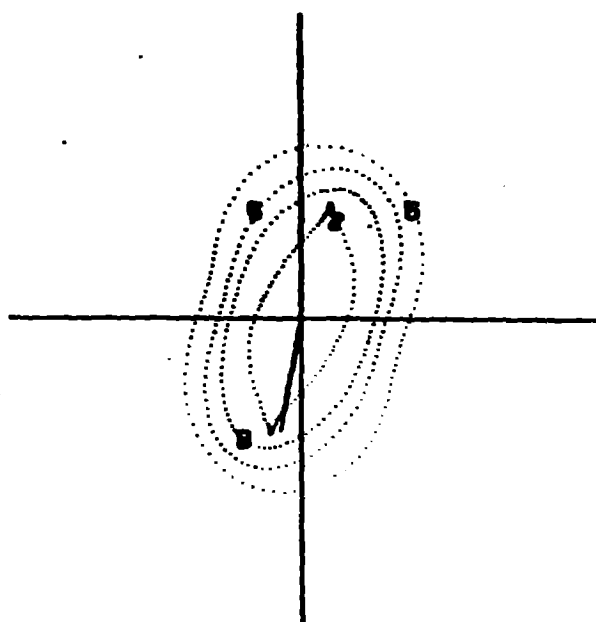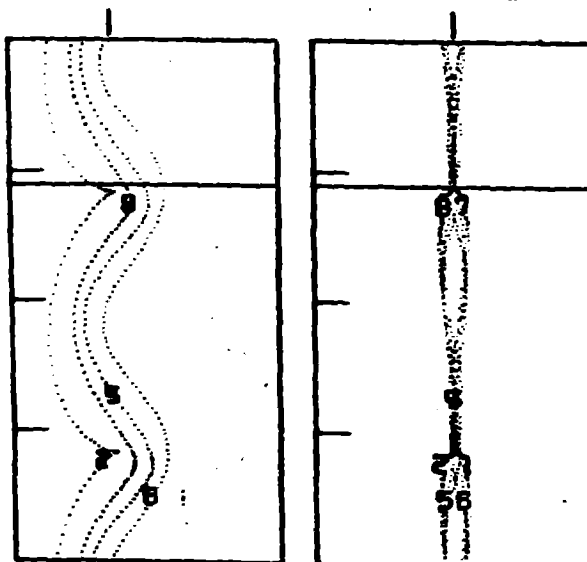Fig. 16. Mean phases versus time for run KRBA ($l = 2$).

Fig. 17. Snapshots of tracer particles for $l = 2$ "radial mode" run at: a) a time halfway through the run; b) the end of the run.
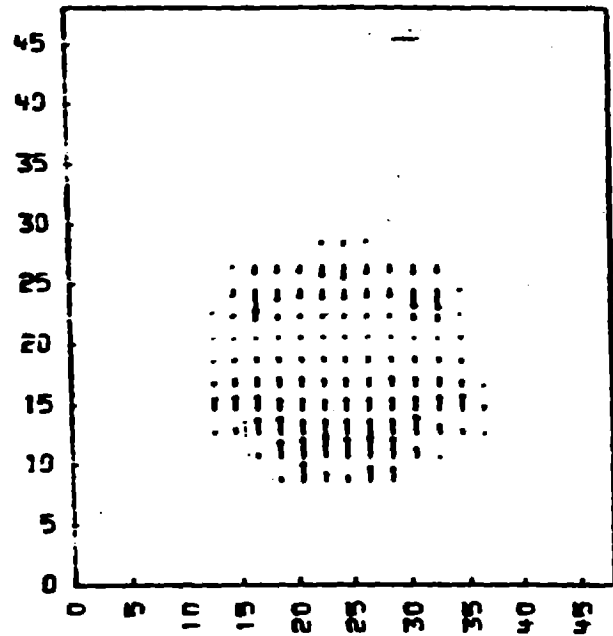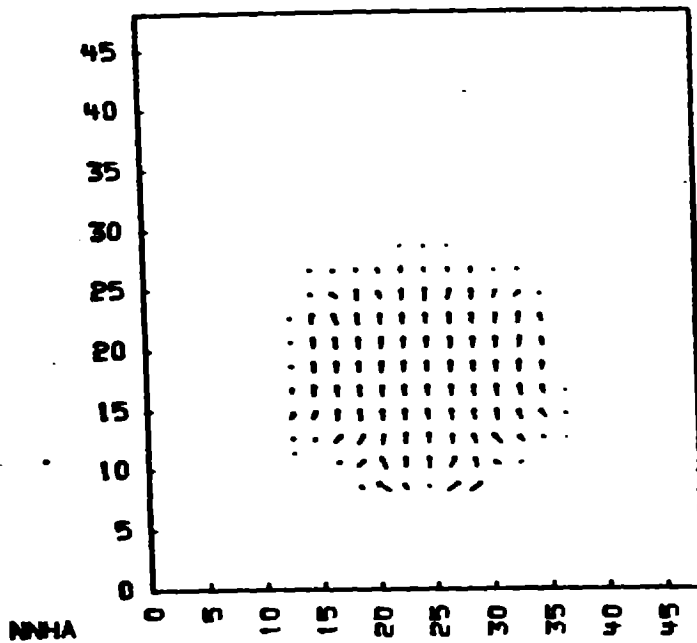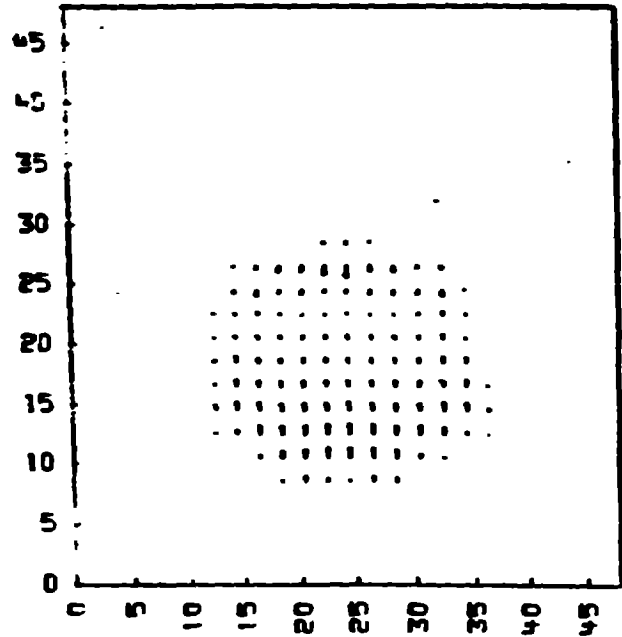
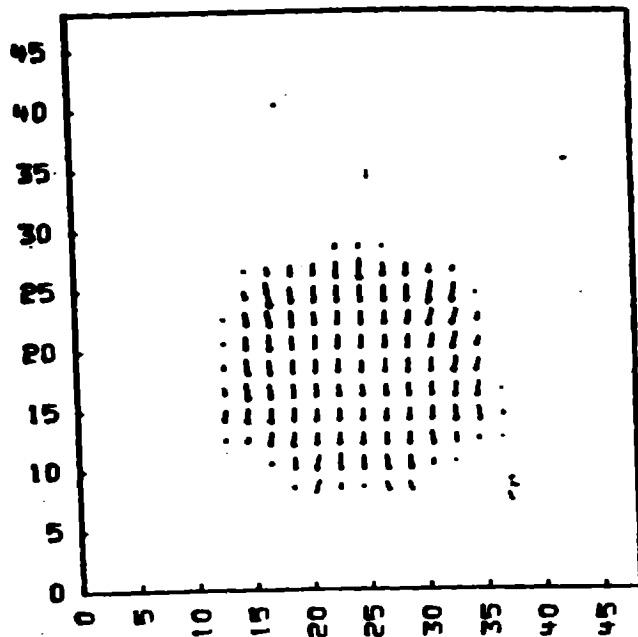Fig. 18. Mean displacements of ring particles at end of $l = 2$ "radial mode" run versus r-z position.

Fig. 19. First order magnetic field versus r-z position for $l = 2$ "radial mode" run.

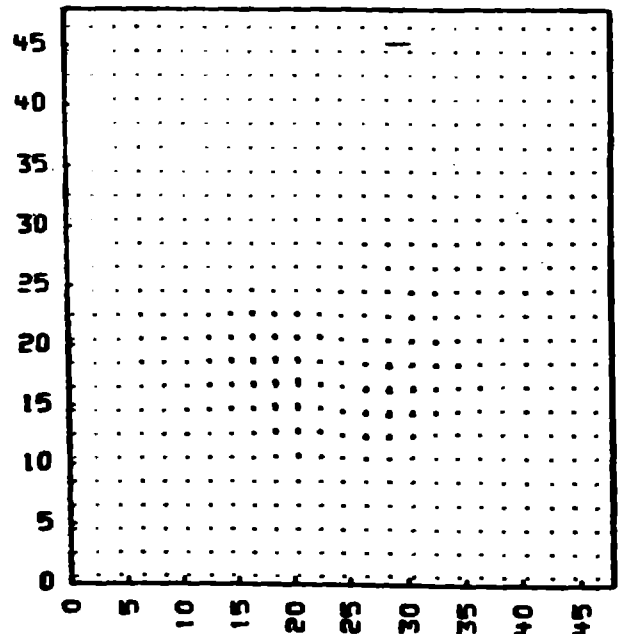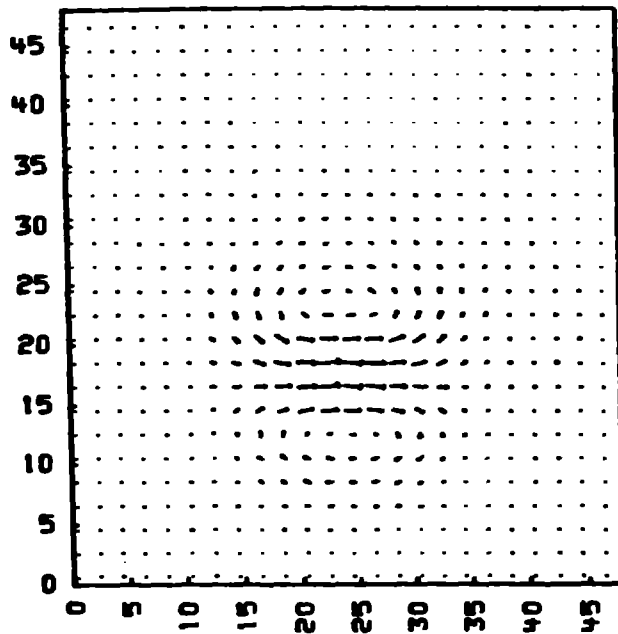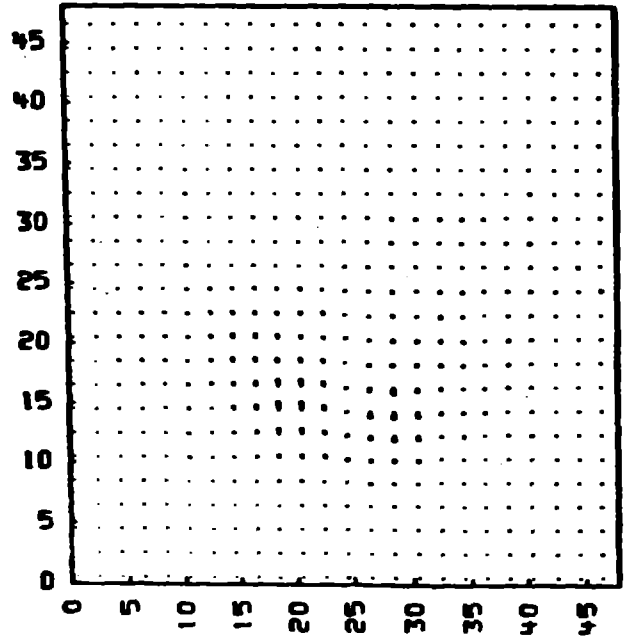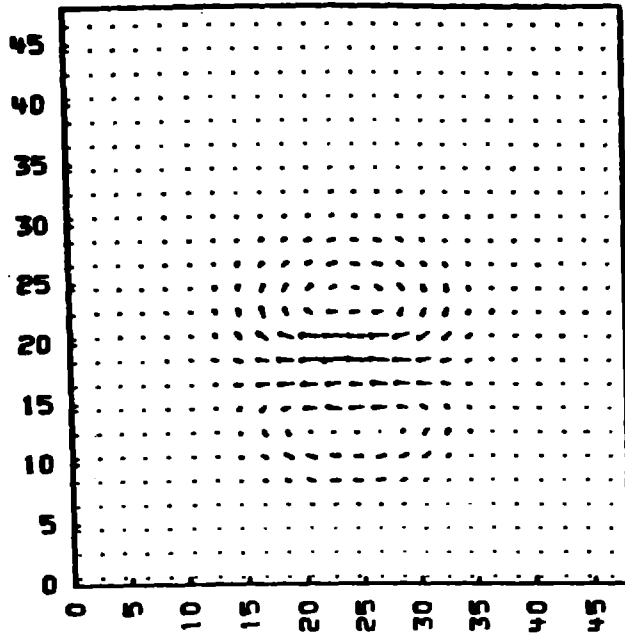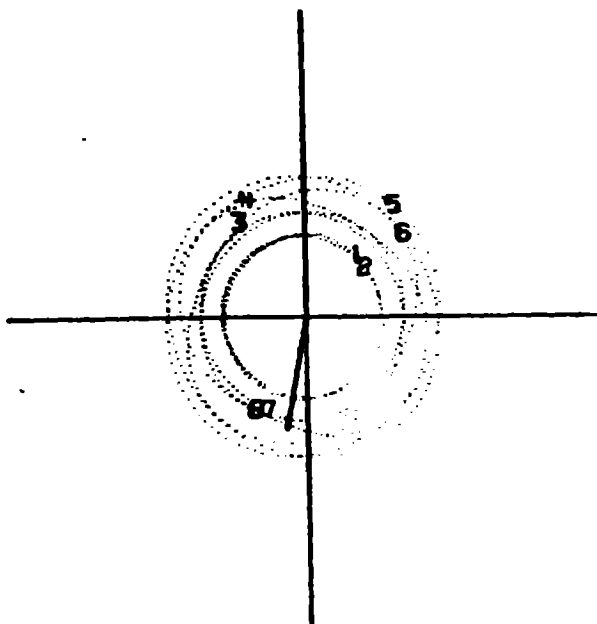Fig. 20. Snapshot of tracer particles for $l = 2$ "axial mode" run, at the end of the run (see text).

Fig. 21. Mean displacements of ring particles at end of $l = 2$ "axial mode" run versus r-z position.

Fig. 22. Mean displacements of ring particles at end of $l = 2$ "axial mode" run versus r and versus z.

Fig. 23. Mean amplitudes versus time for run KRIA ($l = 3$).

Fig. 24. Mean phases versus time for run KRIA ($l = 3$).

Fig. 25. Mean displacements of ring particles at end of $l = 3$ run versus r-z position.

Fig. 26. Mean amplitudes versus time for run KREA ($l = 4$).

Fig. 27. Mean phases versus time for run KREA ($l = 4$).

Fig. 28. Mean amplitudes versus time for run KRFA ($l = 4$, first order Eulerian fields set to zero to illustrate orbit separation in the equilibrium field).

Fig. 29. Mean amplitudes versus time for run KRGA ($l = 5$).

Fig. 30. Mean phases versus time for run KRGA ($l = 5$).

Fig. 31. Mean amplitudes versus time for run KRDA/B ($l = 1$, denser plasma background).

Fig. 32. Mean phases versus time for run KRDA/B ($l = 1$, denser plasma background).

REVERSED MAGNETIC FIELD CONFIGURATION WITH CLOSED FIELD LINES

EXTERNAL MAGNETIC FIELD COILS FOR BASIC MIRROR FIELD

OPEN FIELD LINES
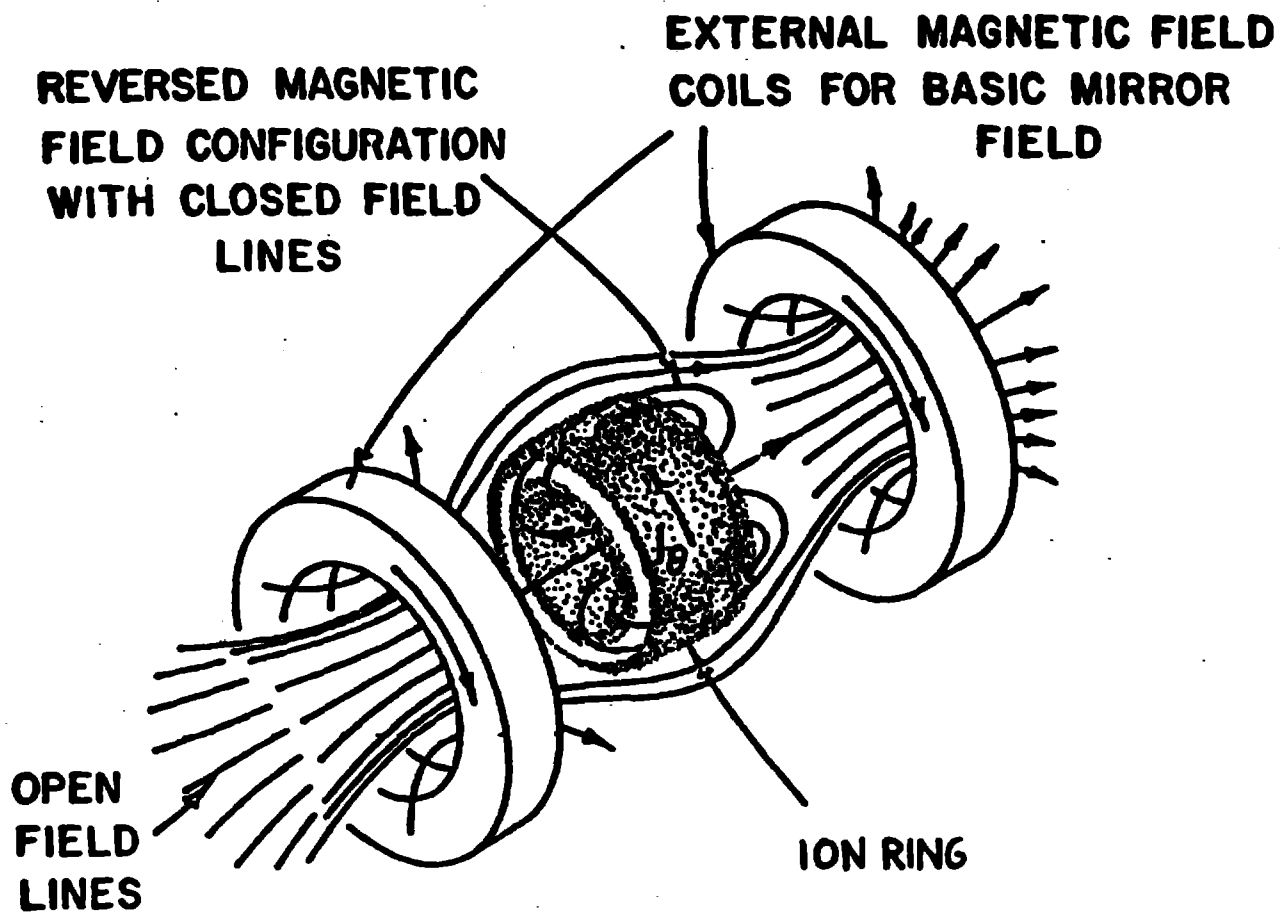
ION RING

Figure 1.

Depiction of field reversed ion ring geometry.
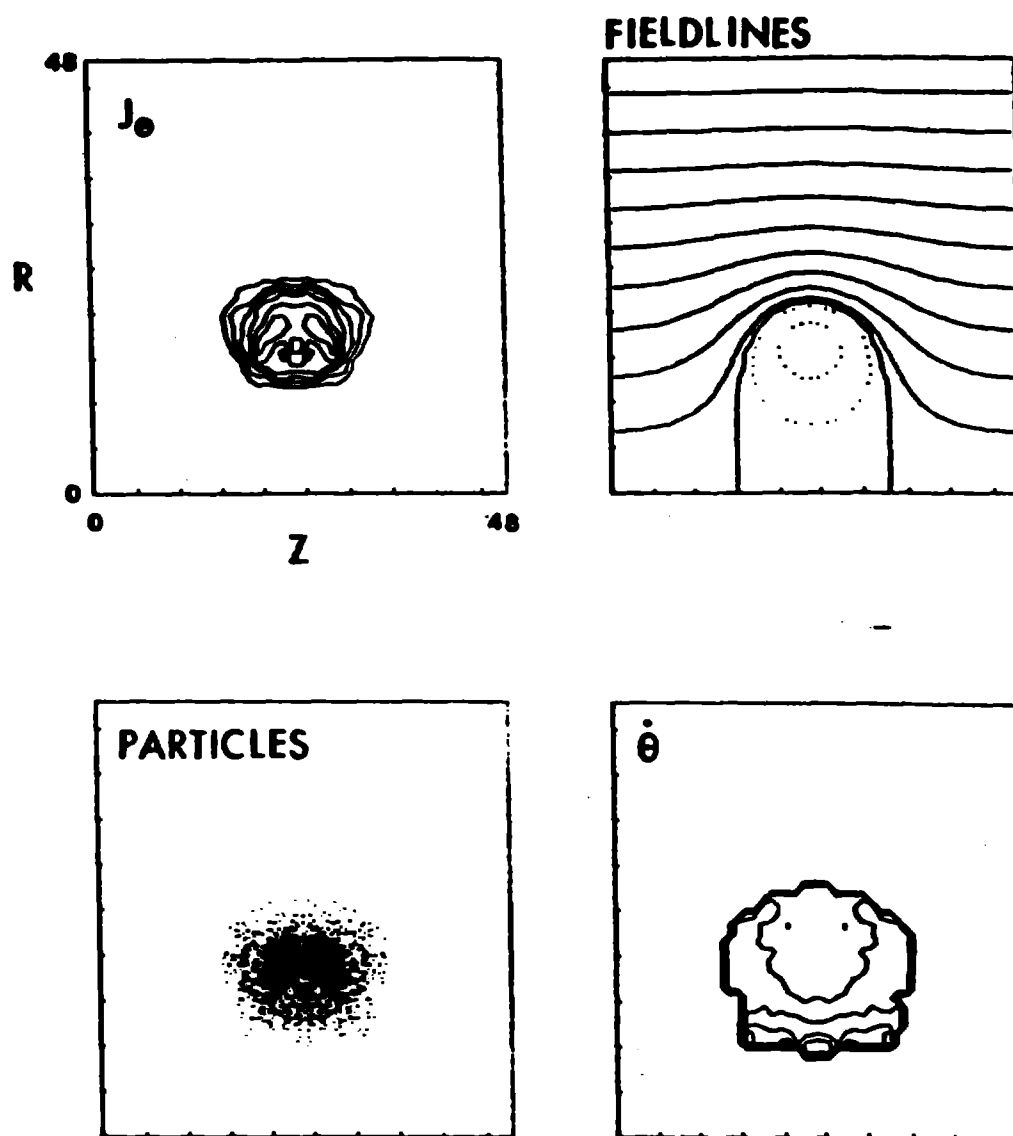
Figure 2.

Clockwise from upper left: contours of $J_{b,\theta}^0$ in r − z plane, fieldlines, contours of mean angular velocity, particle locations, for equilibrium run KR.
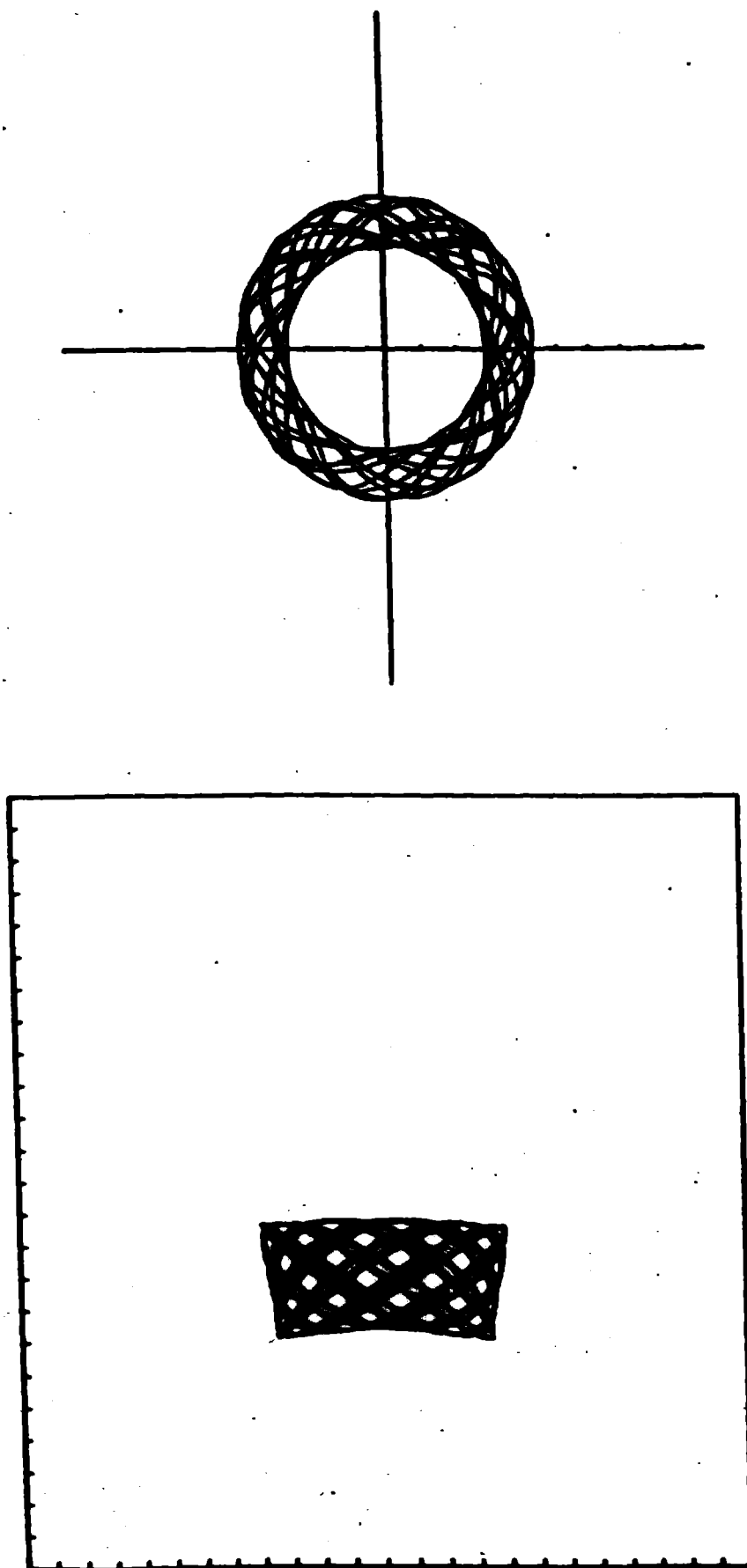
Figure 3.

Typical particle orbit: a) view down axis; b) path in r-z space.
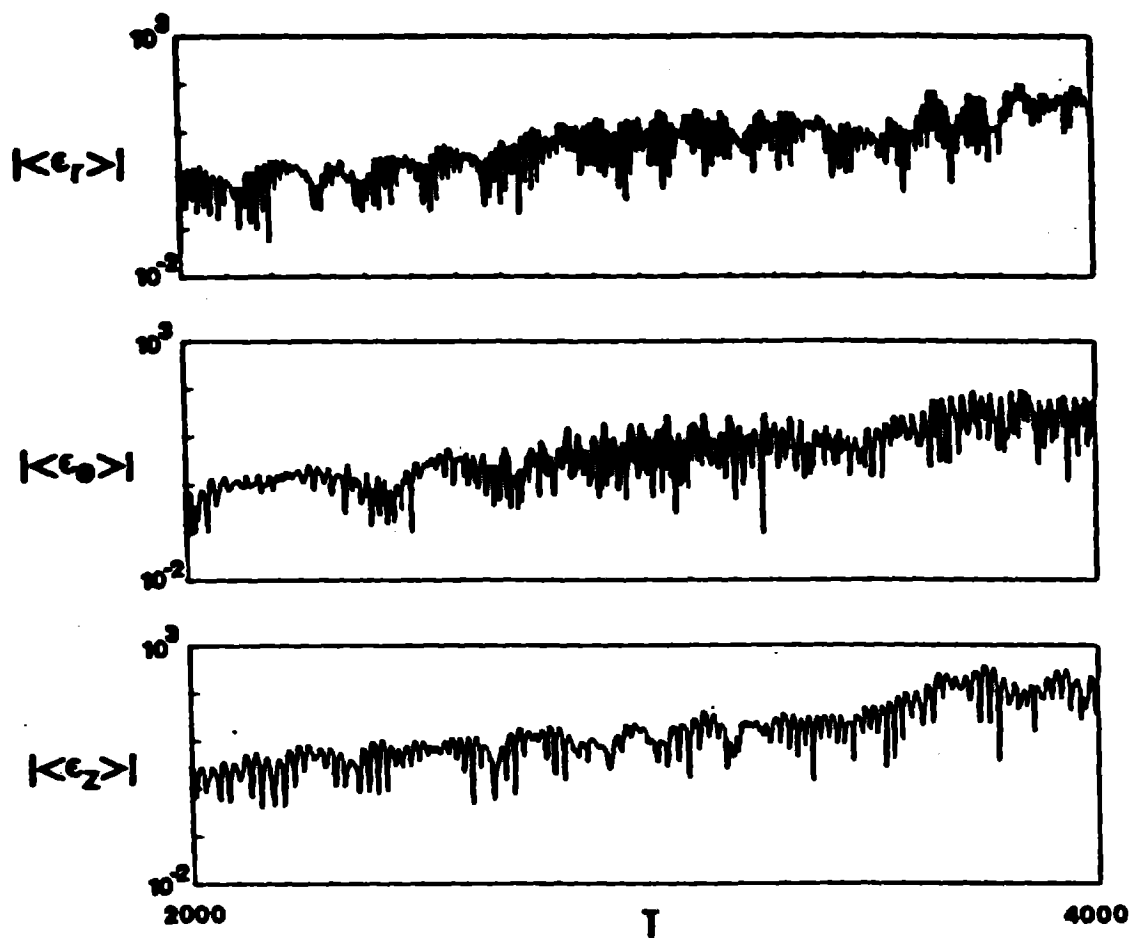
Figure 4.

Amplitudes of components of mean displacement versus time for run KR, with $E^1 = B^1 = 0$. The slow exponential growth reflects the separation of intrinsically stochastic orbits in the equilibrium field.

TRACERS. IT = 0
R VS. THETA

TRACERS. IT = 1000
R VS. THETA

R VS. THETA   Z VS. THETA

360°

0°

R VS. THETA   Z VS. THETA

a

b
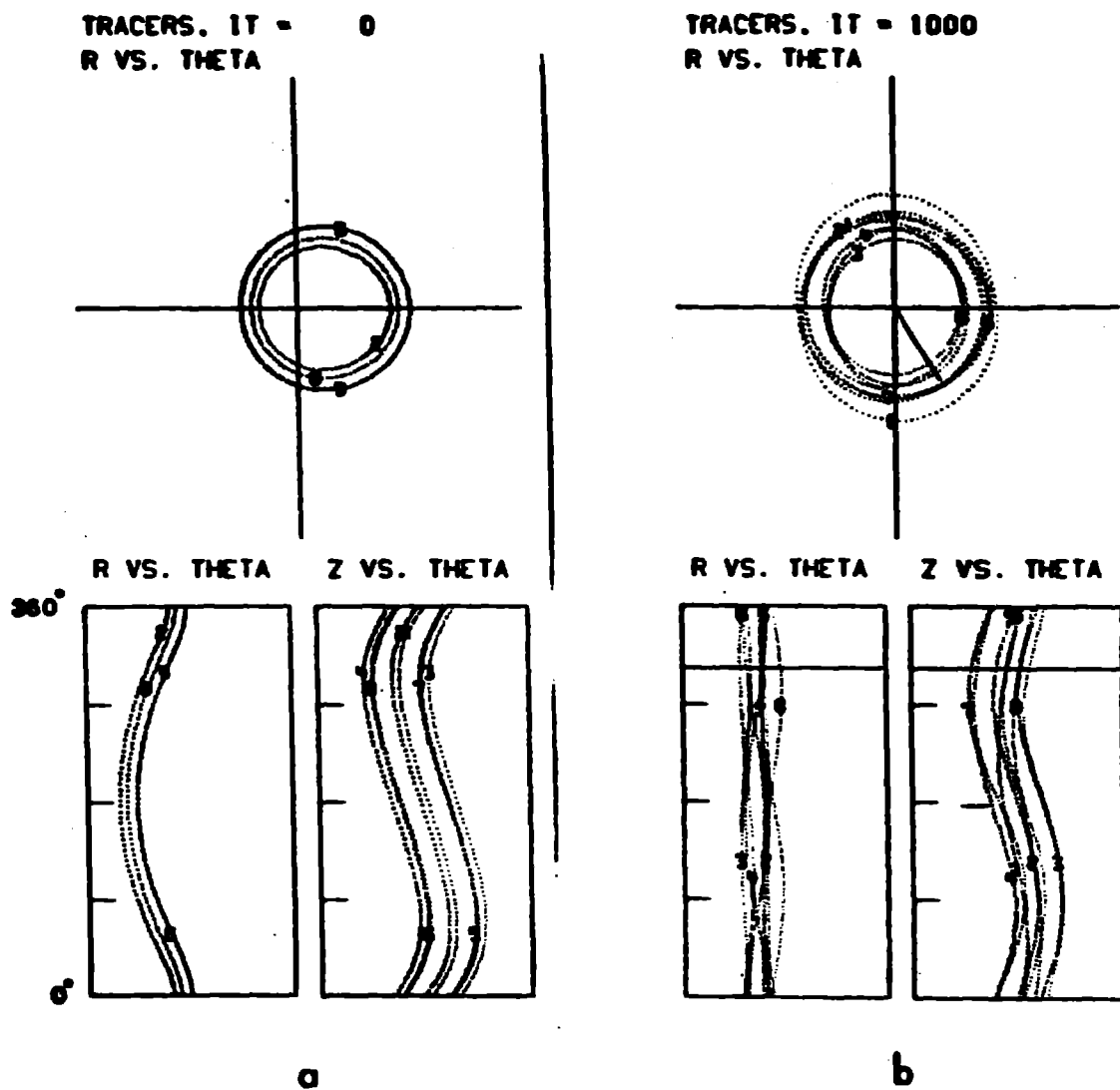
Figure 5.

Snapshots of tracer particles for run KRAA. (a) Timestep 0. (b)
Timestep 1000.
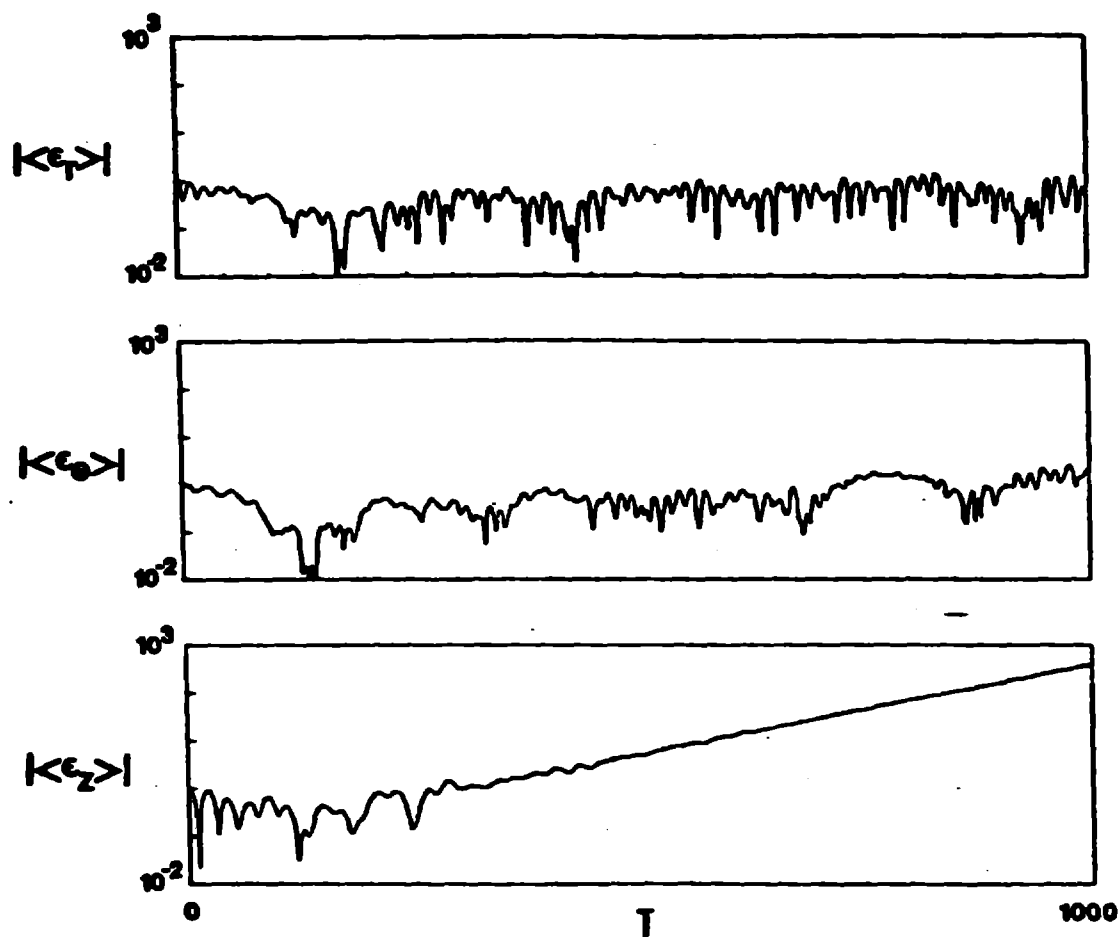
Figure 6.

Mean amplitudes of radial, azimuthal, and axial components of particle displacements versus time for run KRAA ($l = 1$).
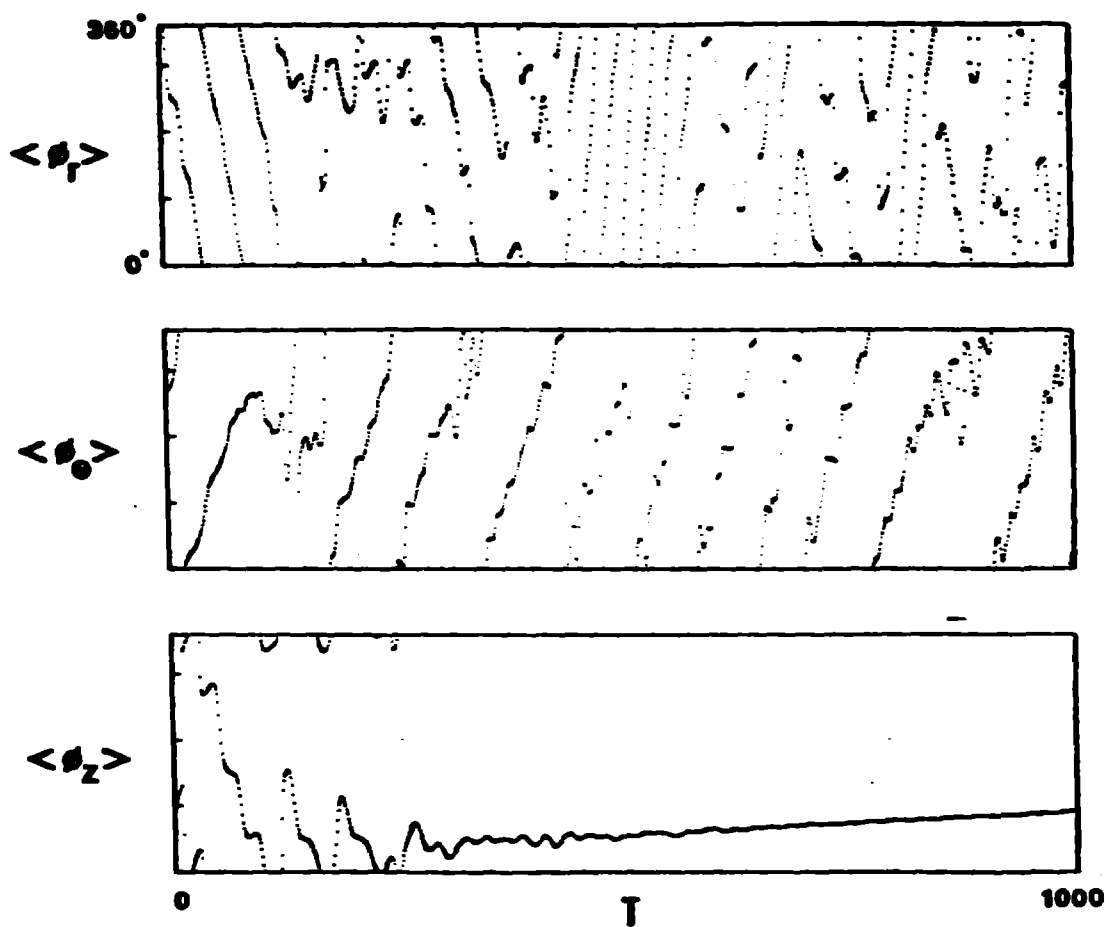
Figure 7.

Mean phases of radial, azimuthal, and axial components of particle
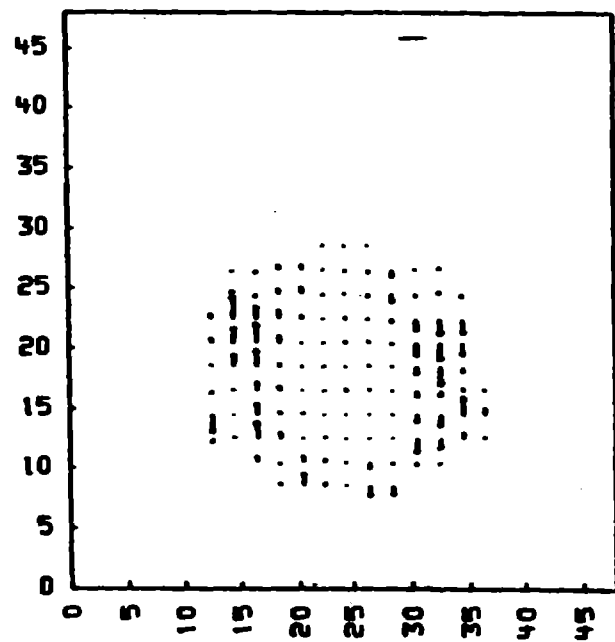displacements versus time for run KRAA ($l = 1$).
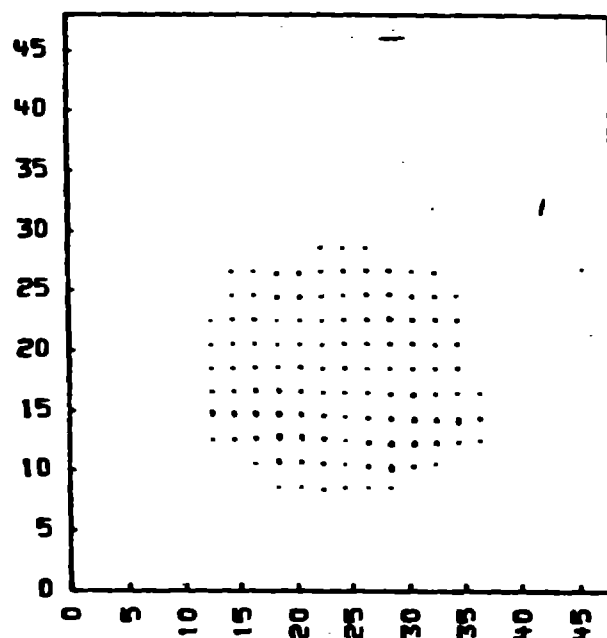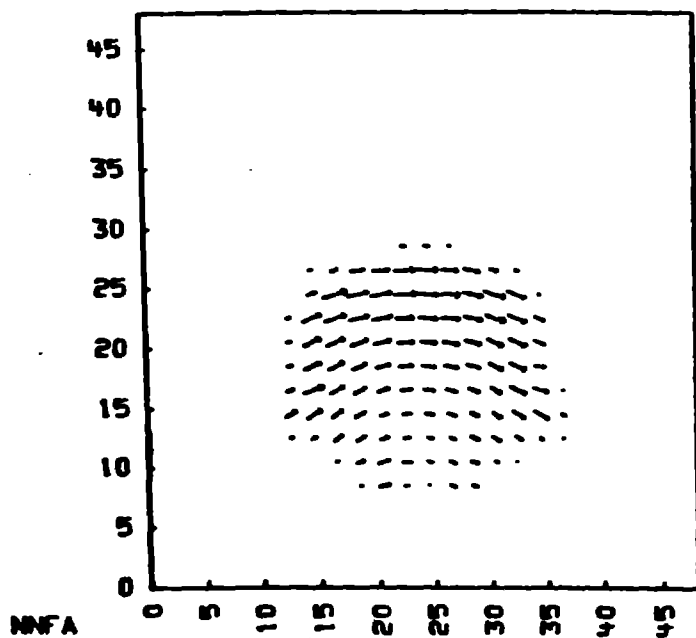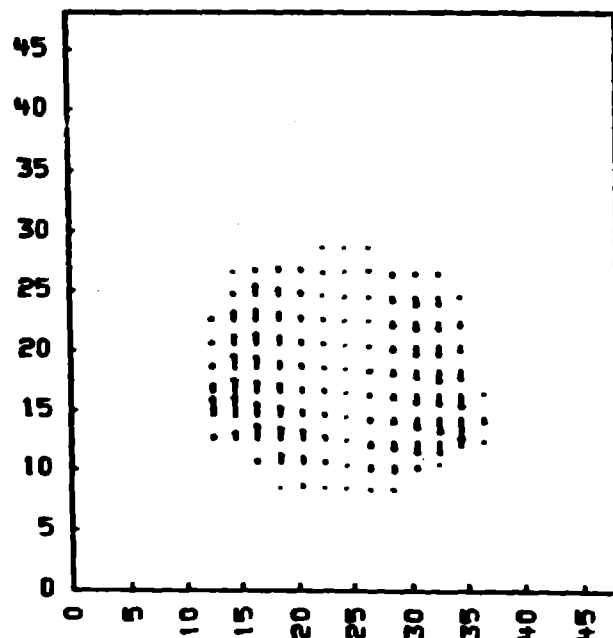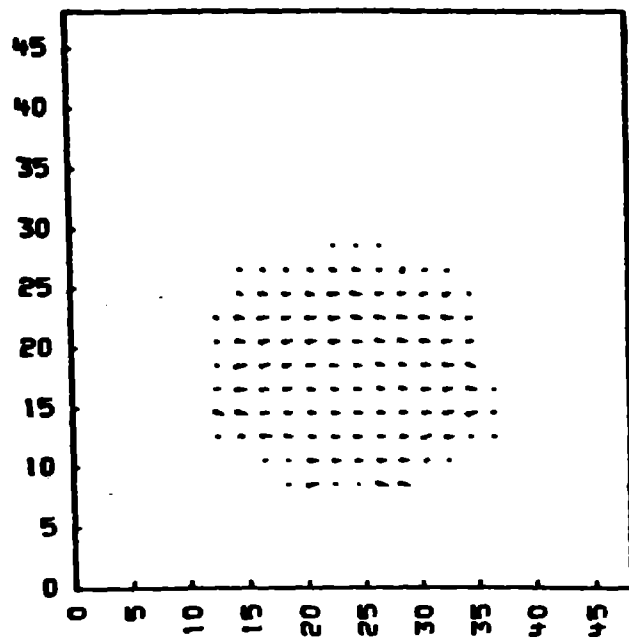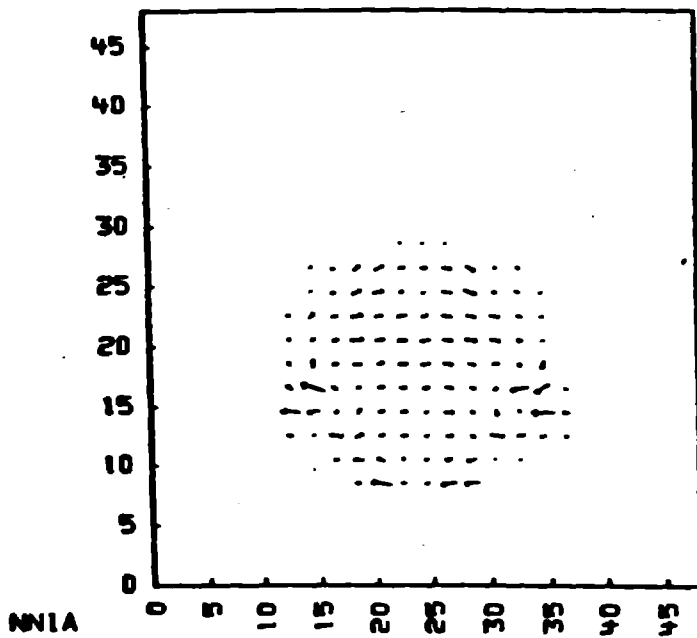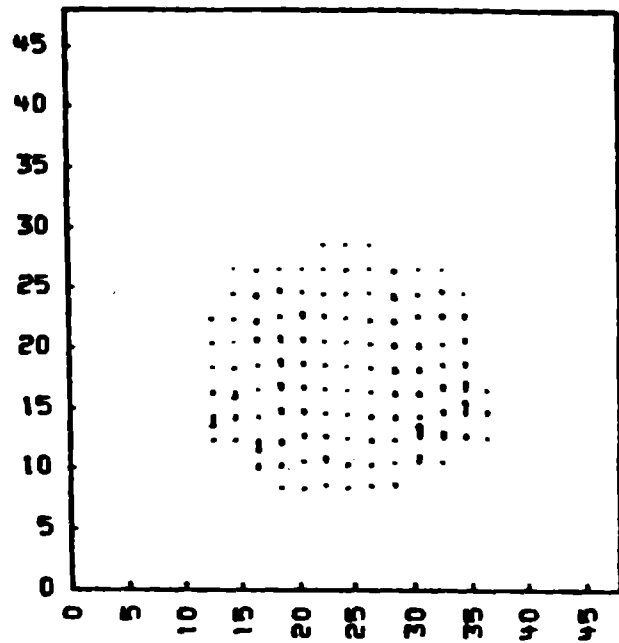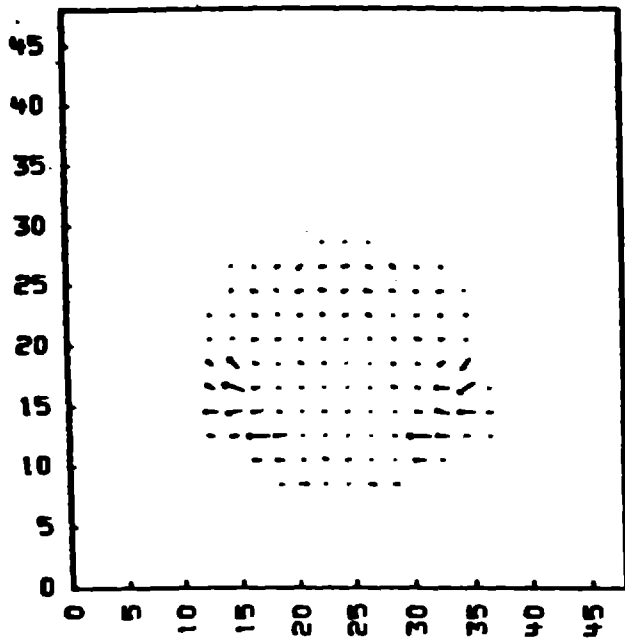
Figure 8.

Mean displacements of ring particles at end of $l = 1$ run versus r-z position (see text).

MEAN EPSILONS   IT = 2000
-R1,2 -T1,2 -Z1,2 VS R,Z   R = 17.5
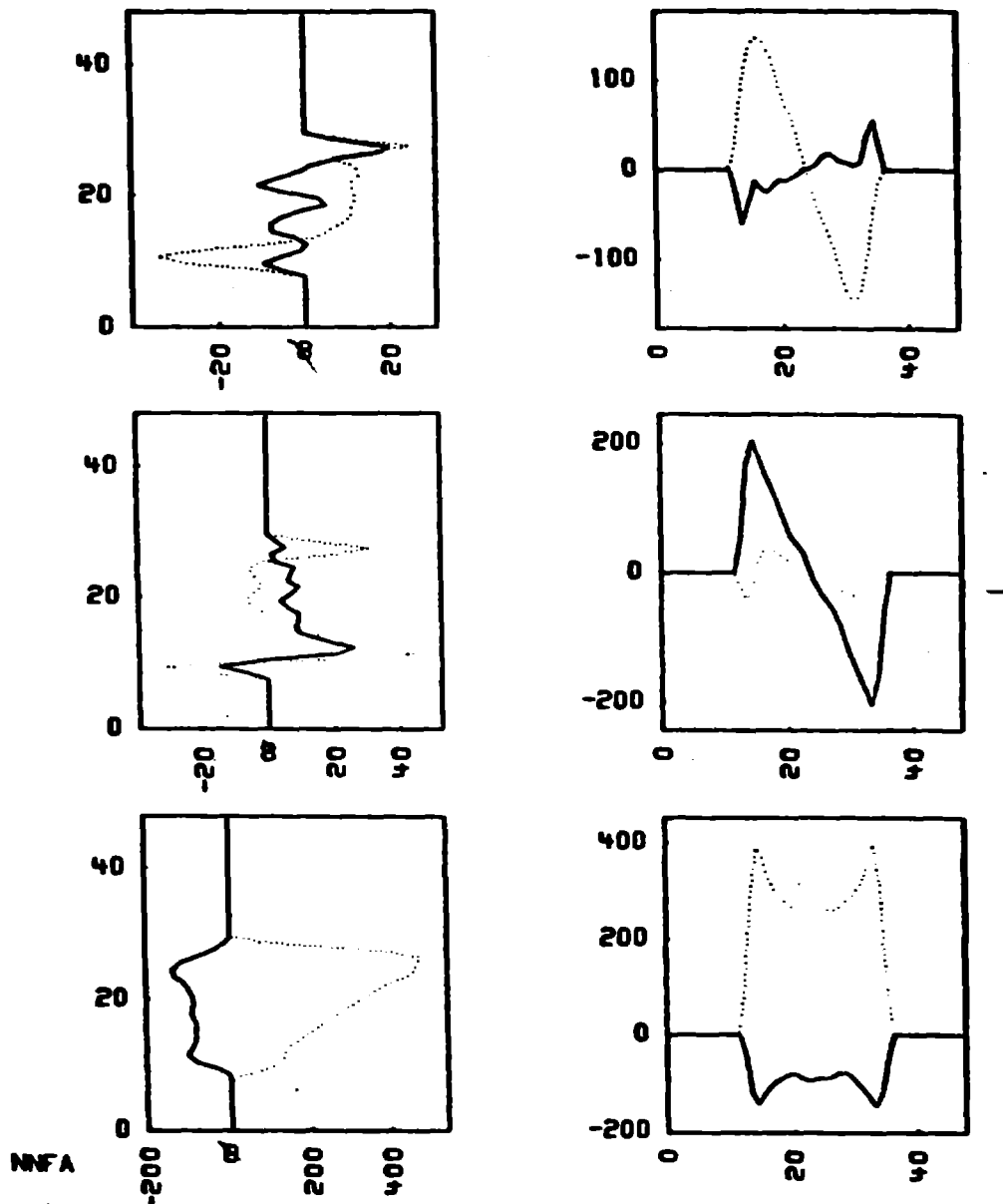
Figure 9.

Mean displacements of ring particles for $l = 1$ versus r and versus z
(see text).
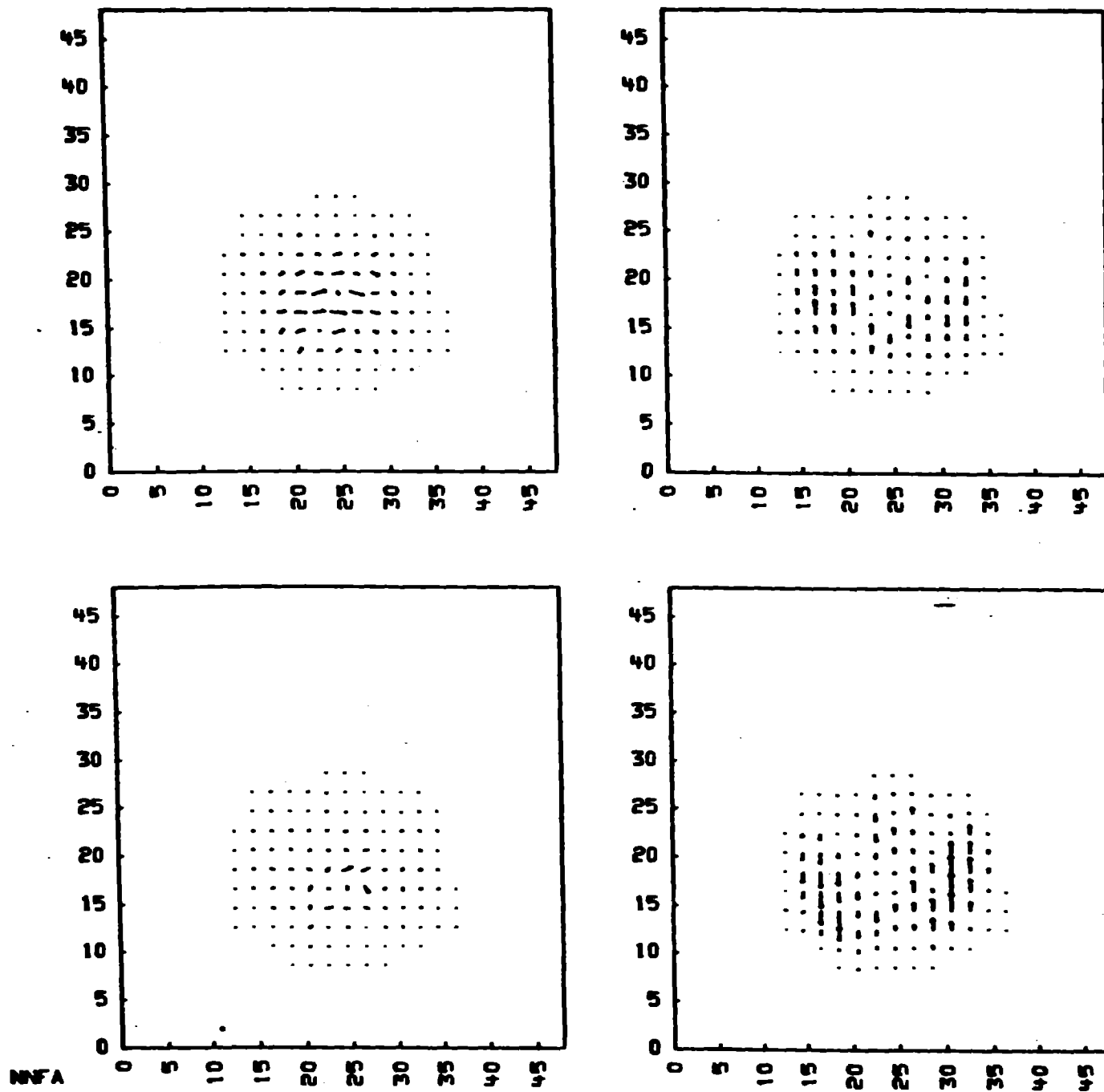
Figure 10.

First order beam current versus r-z position for $l = 1$.

FIRST ORDER BEAM CURRENT IT = 2000
−R1,2 −T1,2 −Z1,2 VS R,Z   R = 17.5
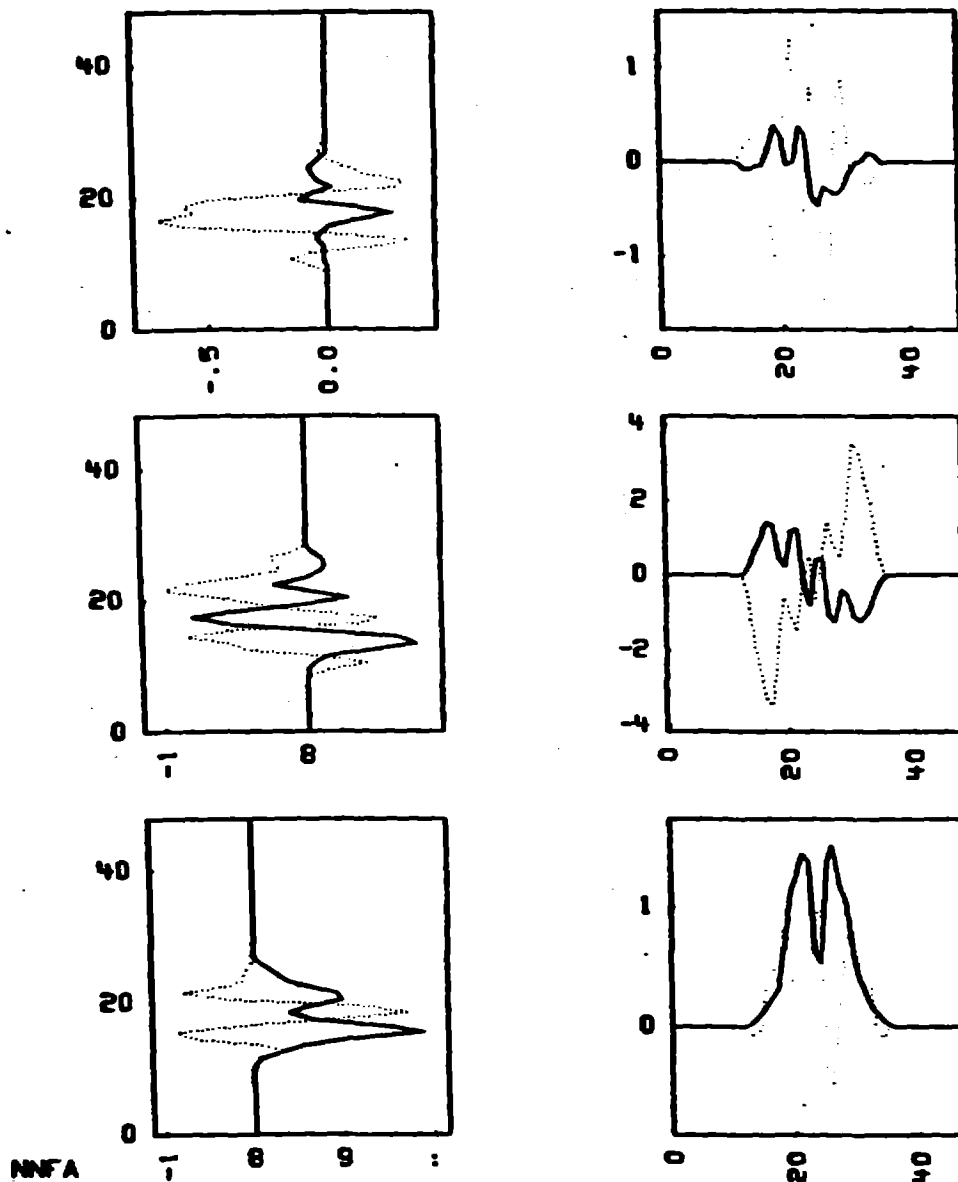
Figure 11.

First order beam current versus r and versus z for $l = 1$.

IT = 2000 FIRST ORDER MAGNETIC FIELD
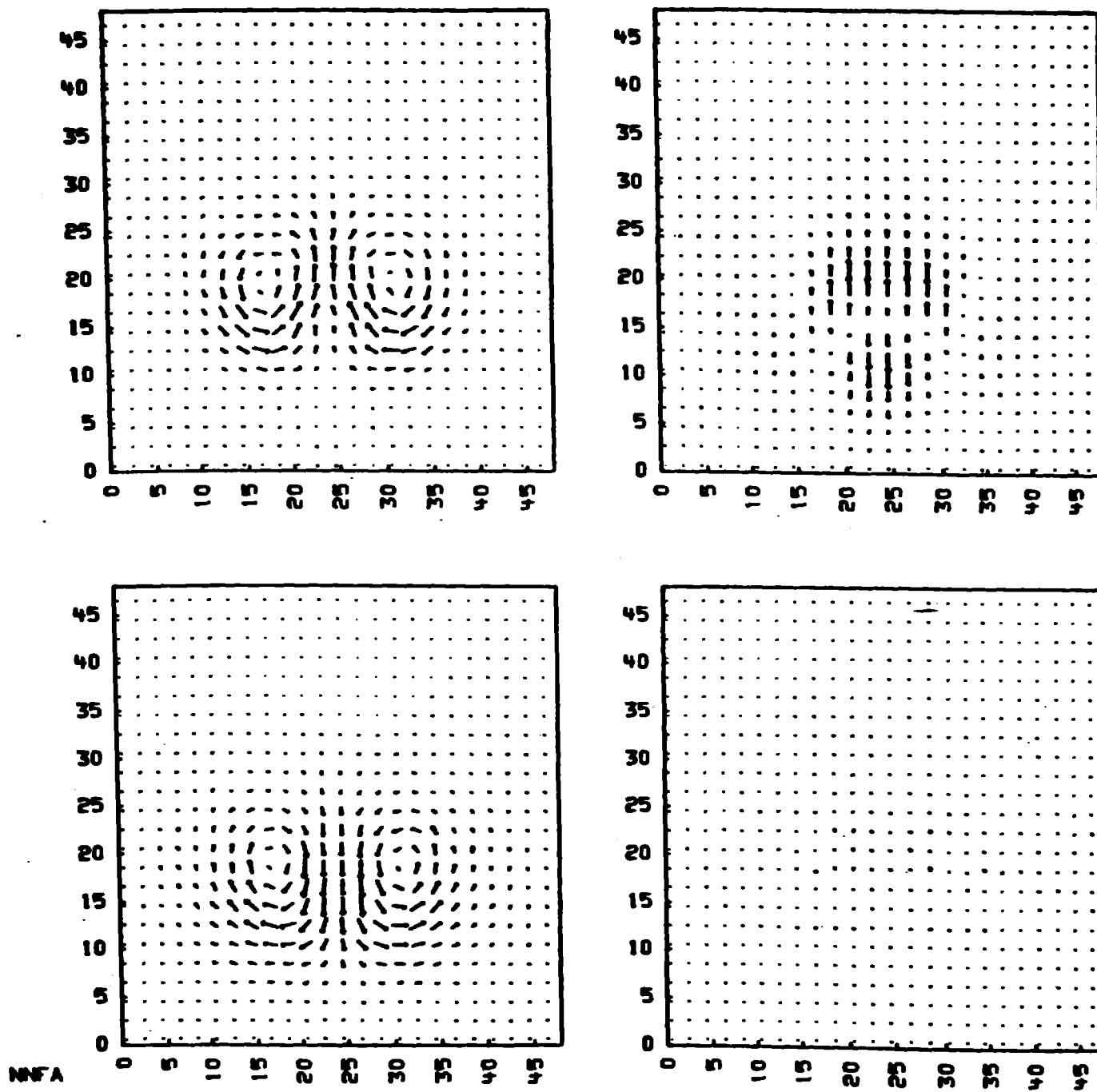
Figure 12.

First order magnetic field versus r-z position for l = 1.

IT = 2000   FIRST ORDER PLASMA ION J
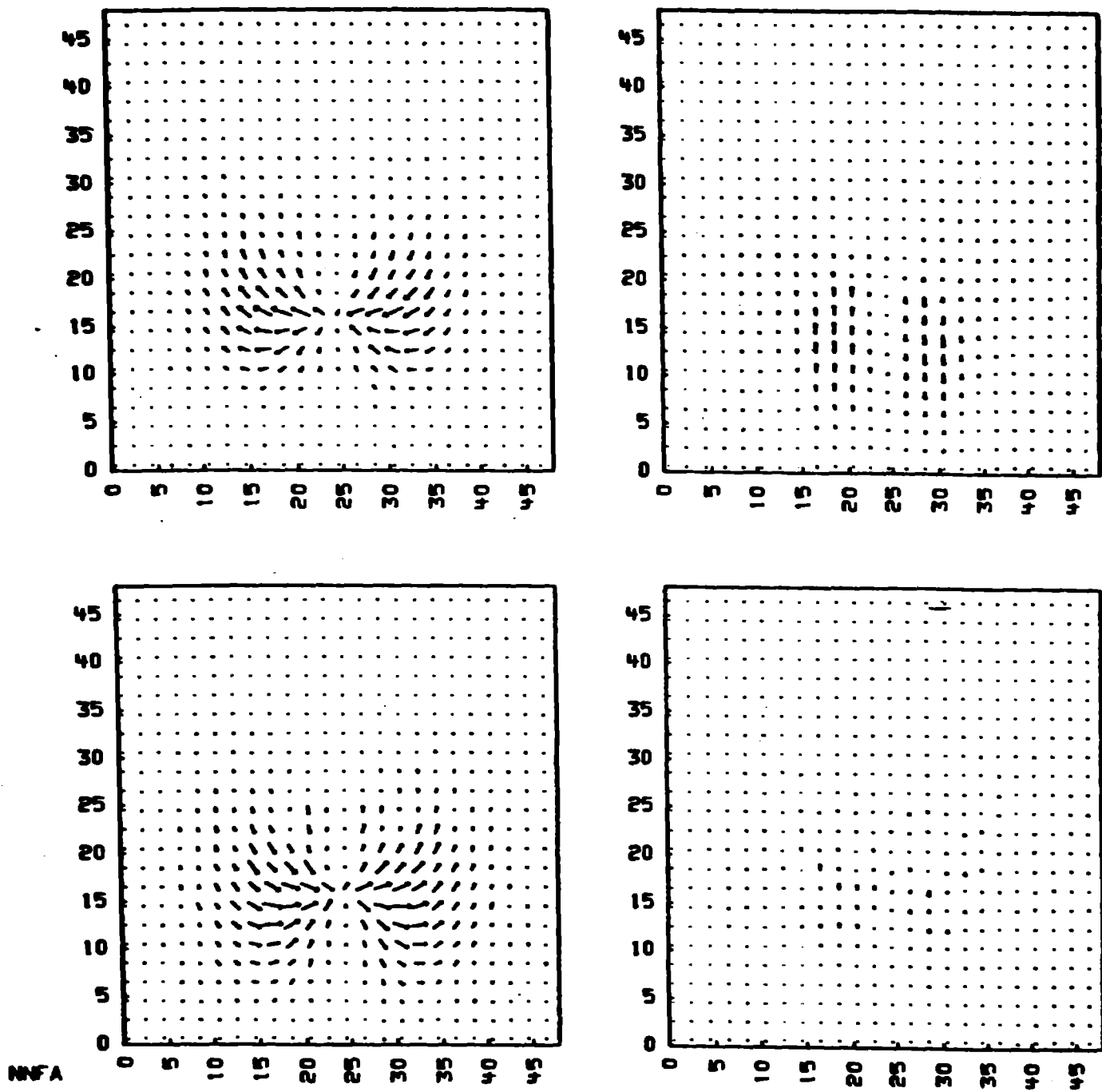
Figure 13.

First order plasma ion current versus r-z position for $l = 1$.

IT = 2000   J TOTAL FROM CURL B1.2

Figure 14.

First order total current versus r-z position for $\ell = 1$.
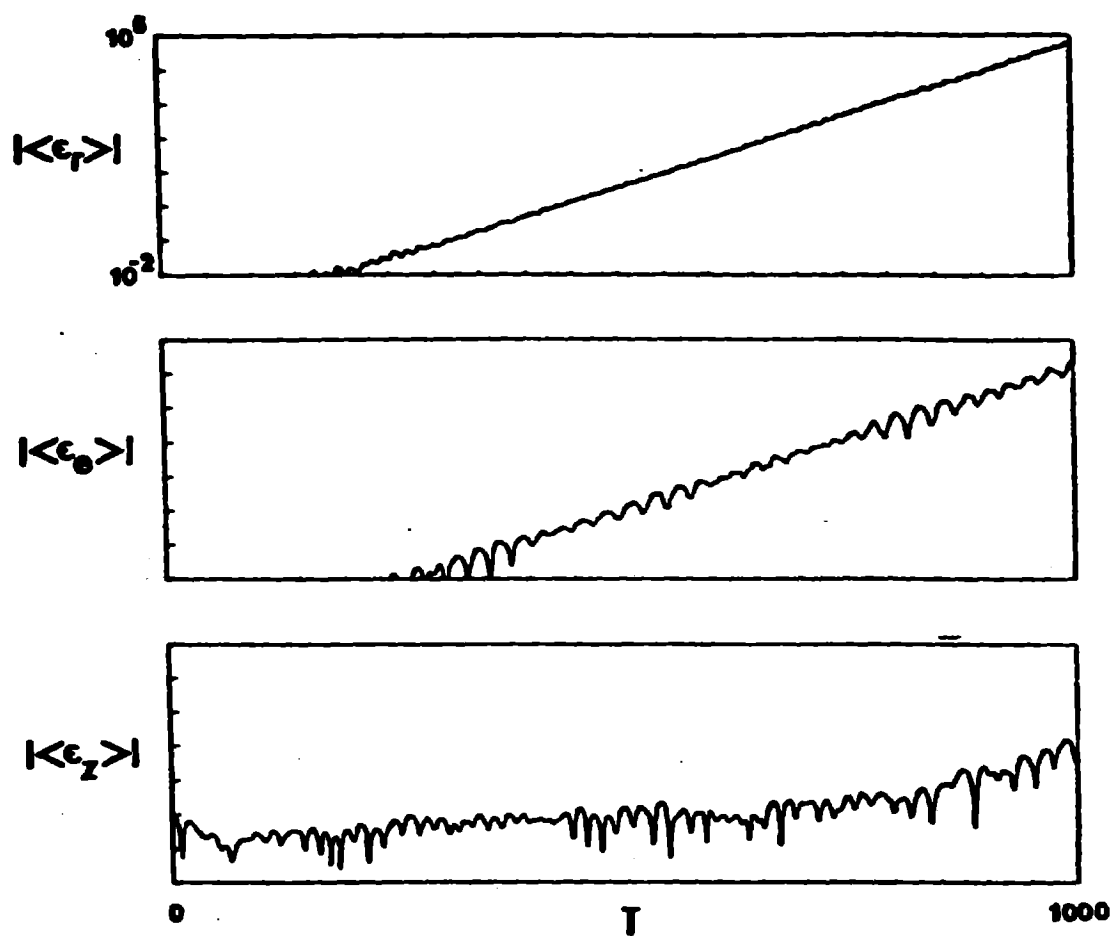
Figure 15.

Mean amplitudes versus time for run KRBA ($l = 2$).

Figure 16.

Mean phases versus time for run KRBA ($l = 2$).

TRACERS. IT = 1500
R VS. THETA

TRACERS. IT = 2000
R VS. THETA

R VS. THETA   Z VS. THETA
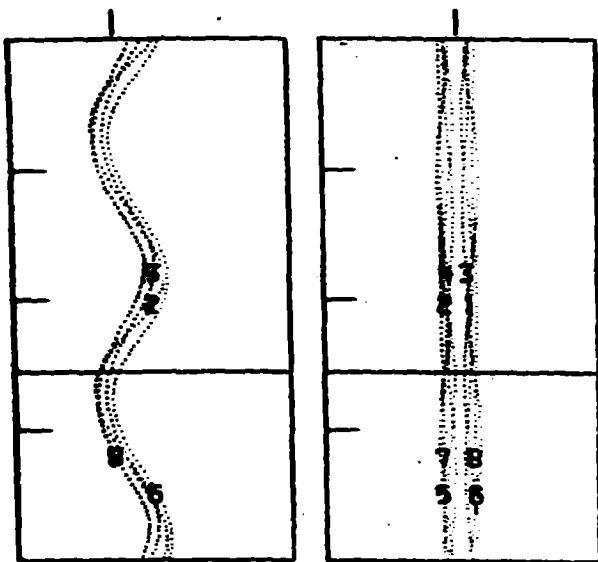
R VS. THETA   Z VS. THETA

Figure 17.

Snapshots of tracer particles for $\ell = 2$ "radial mode" run at: a) a time
halfway through the run; b) the end of the run.

Figure 18.

Mean displacements of ring particles at end of $\ell = 2$ "radial mode" run versus r-z position.

IT = 2000   FIRST ORDER MAGNETIC FLD

Figure 19.

First order magnetic field versus r-z position for $l = 2$ "radial mode" run.

TRACERS. IT = 2000
R VS. THETA

PERTURBATION MAXIMUM = 1.639E+06
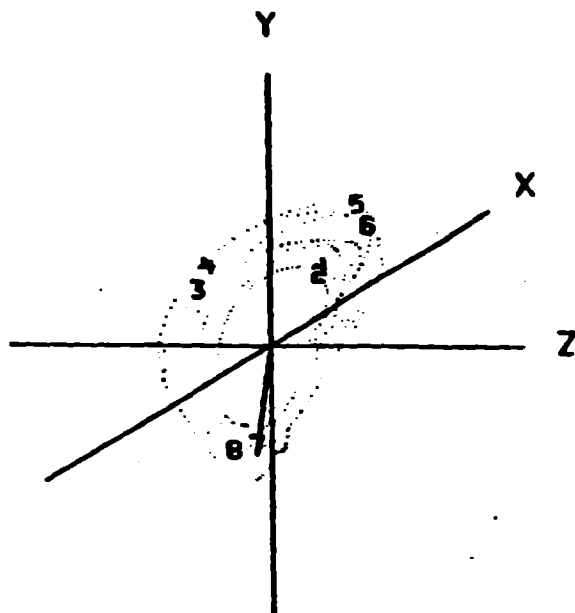
R VS. THETA   Z VS. THETA

R VS. Z. SECTIONS

NNIA

-5 -4 -3 -2 -1 0 1 2 3 4 5 6 7 8 9 10
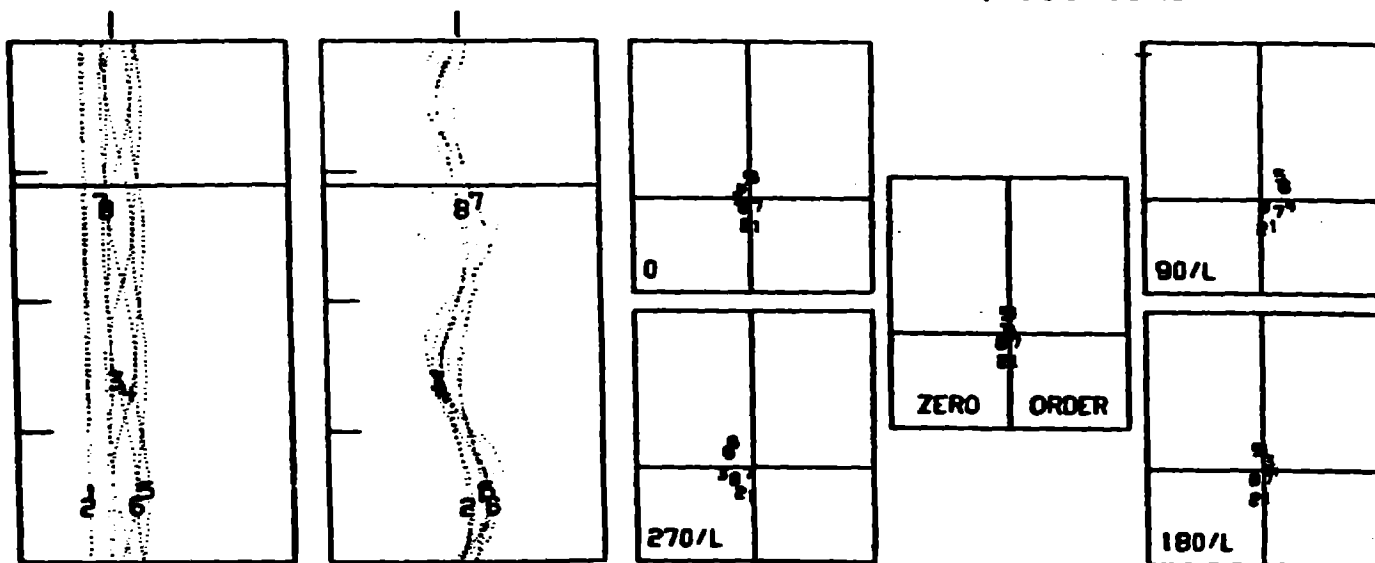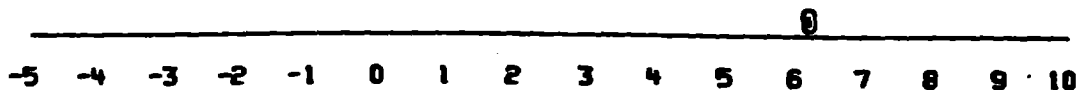
Figure 20.

Snapshot of tracer particles for $l = 2$ "axial mode" run, at the end of the run (see text).

IT = 2000   MEAN EPSILONS

Figure 21.

Mean displacements of ring particles at end of $l = 2$ "axial mode" run versus r-z position.

MEAN EPSILONS   IT = 2000

-R1,2 -T1,2 -Z1,2 VS R,Z   R = 17.5
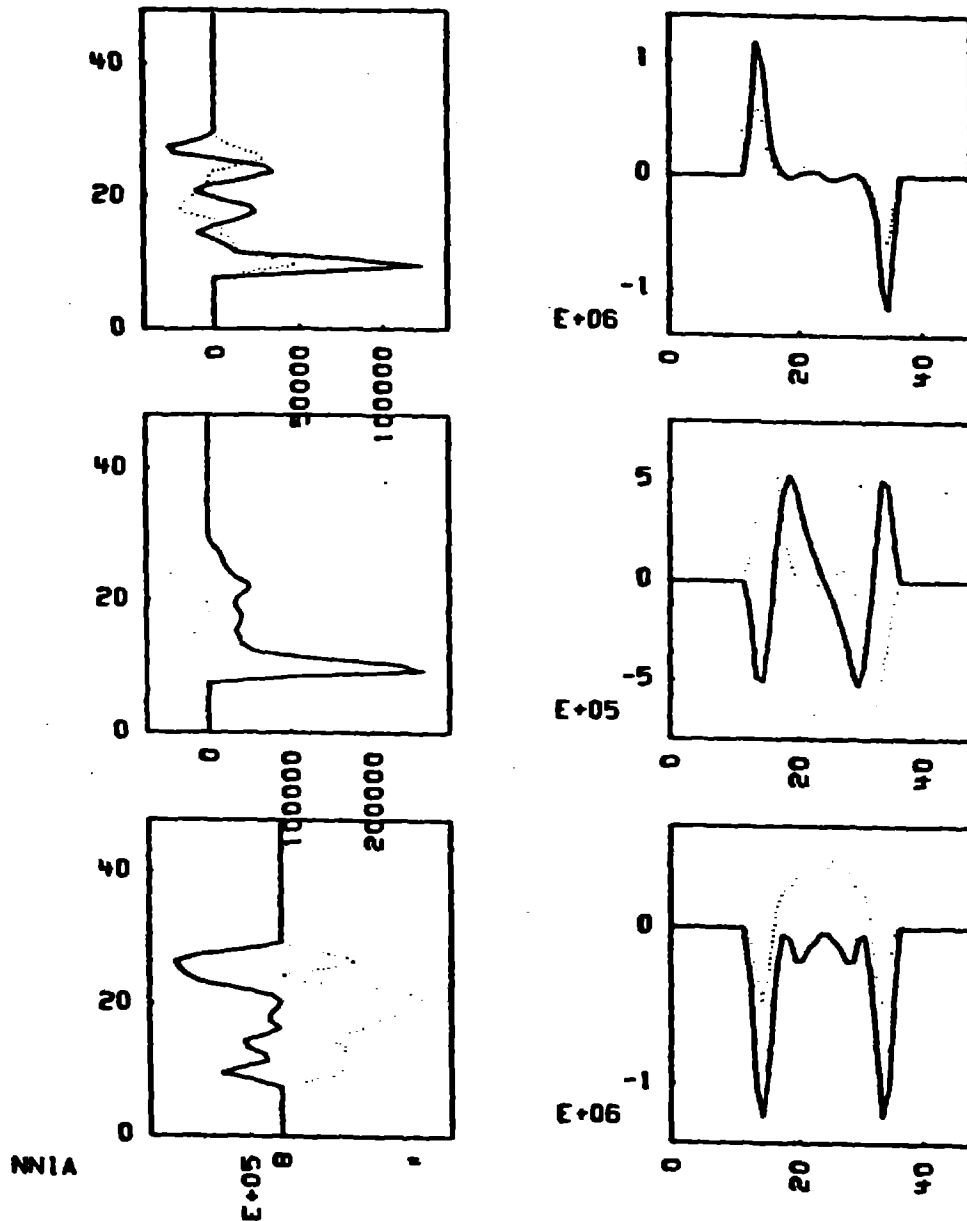
Figure 22.

Mean displacements of ring particles at end of $l = 2$ "axial mode" run versus r and versus z.

Figure 23.

Mean amplitudes versus time for run KRIA ($l = 3$).
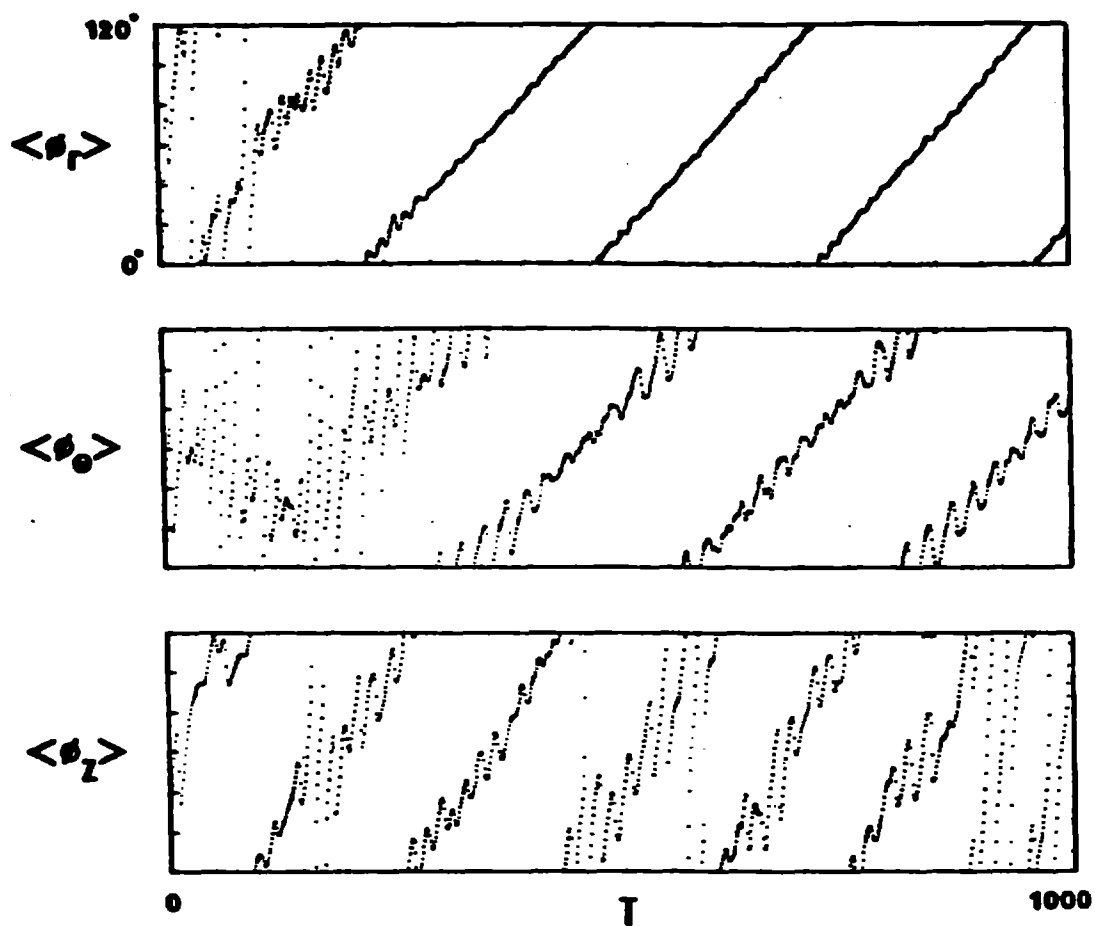
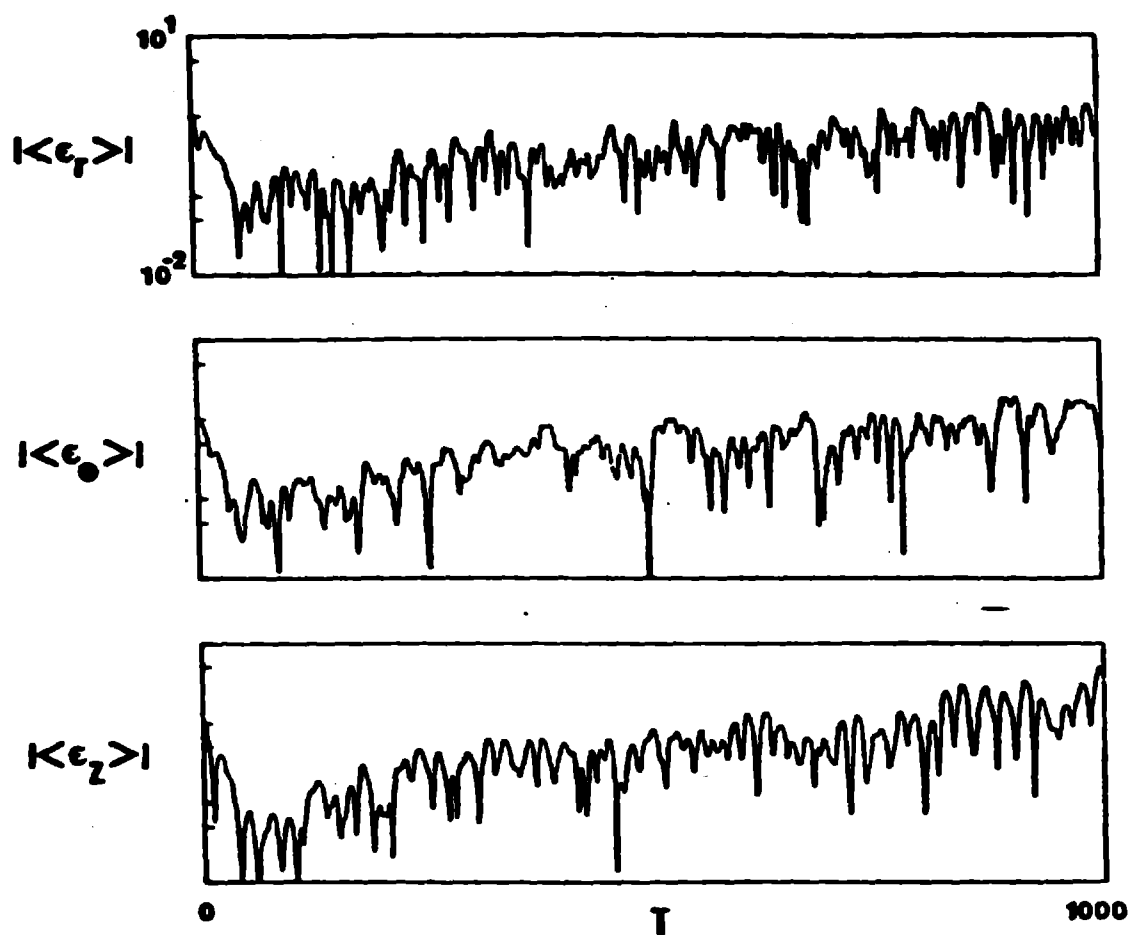Figure 24.

Mean phases versus time for run KRIA ($l = 3$).
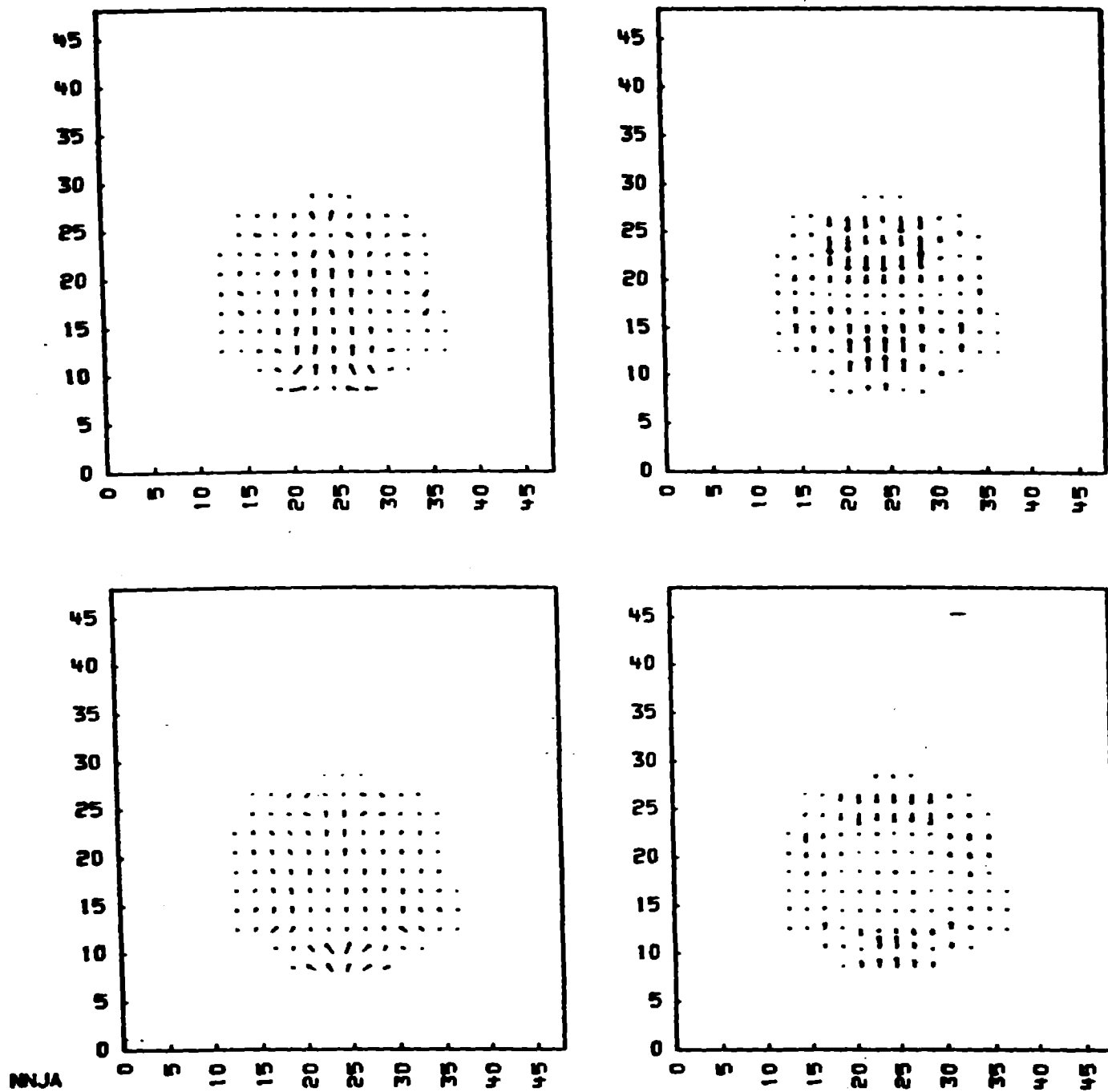
Figure 25.

Mean displacements of ring particles at end of $l = 3$ run versus r-z position.
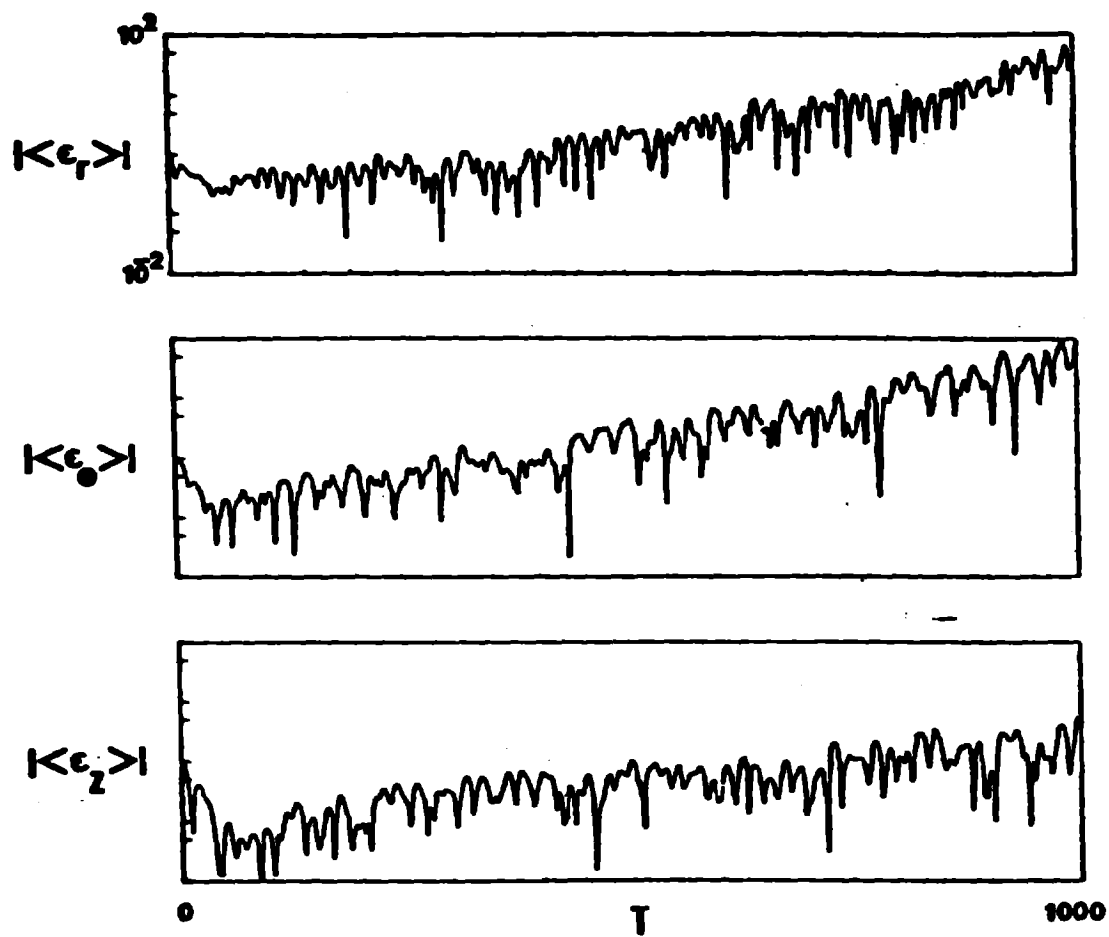
Figure 26.

Mean amplitudes versus time for run KREA ($l = 4$).
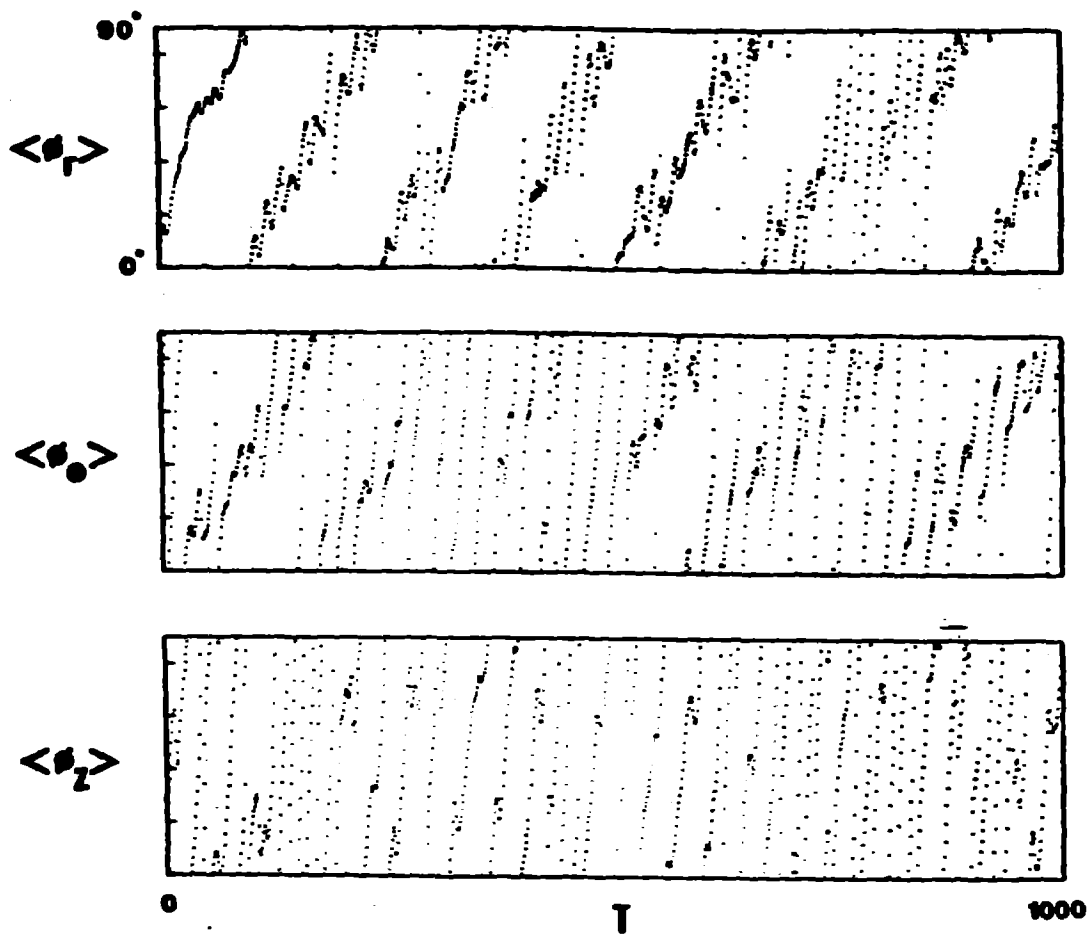
Figure 27.

Mean phases versus time for run KREA ($l = 4$).

Figure 28.

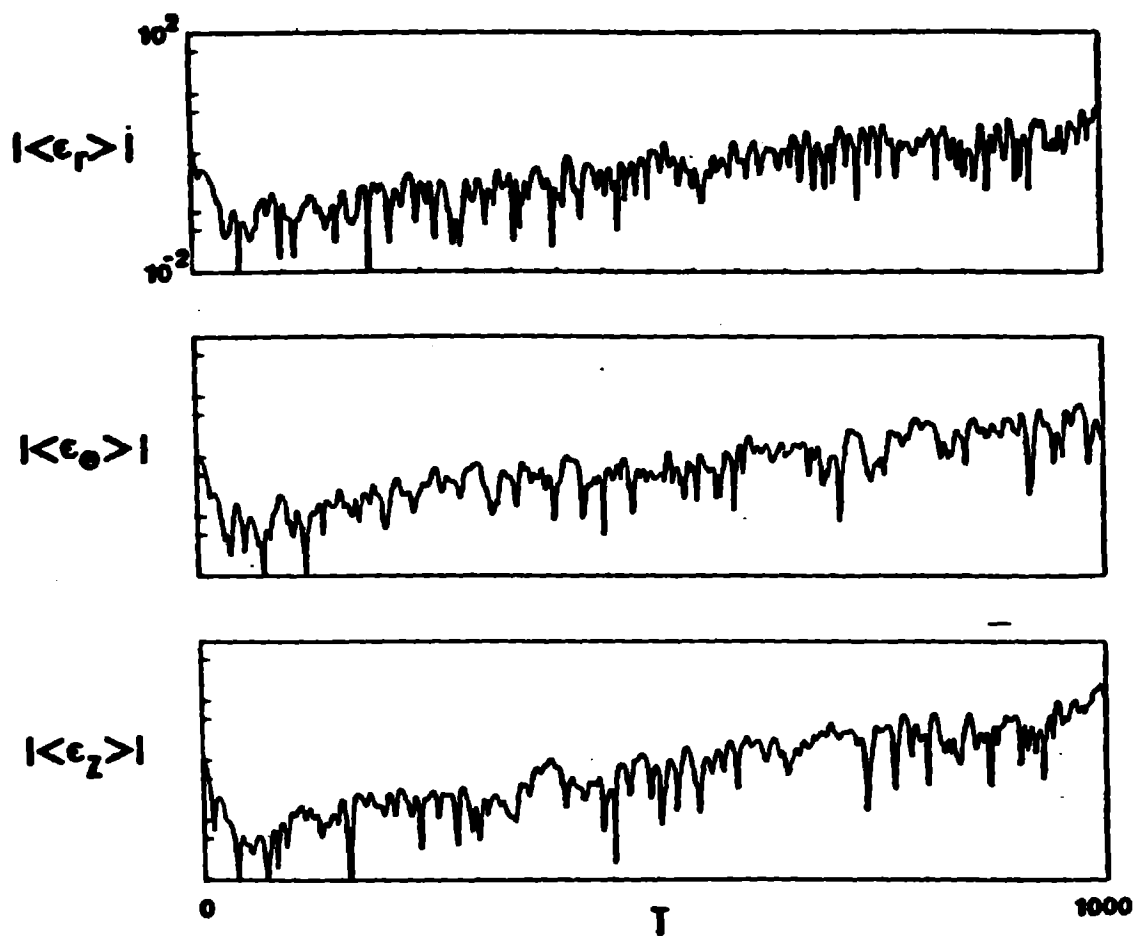Mean amplitudes versus time for run KRFA ($l = 4$, first order Eulerian fields set to zero to illustrate orbit separation in the equilibrium field).

Figure 29.

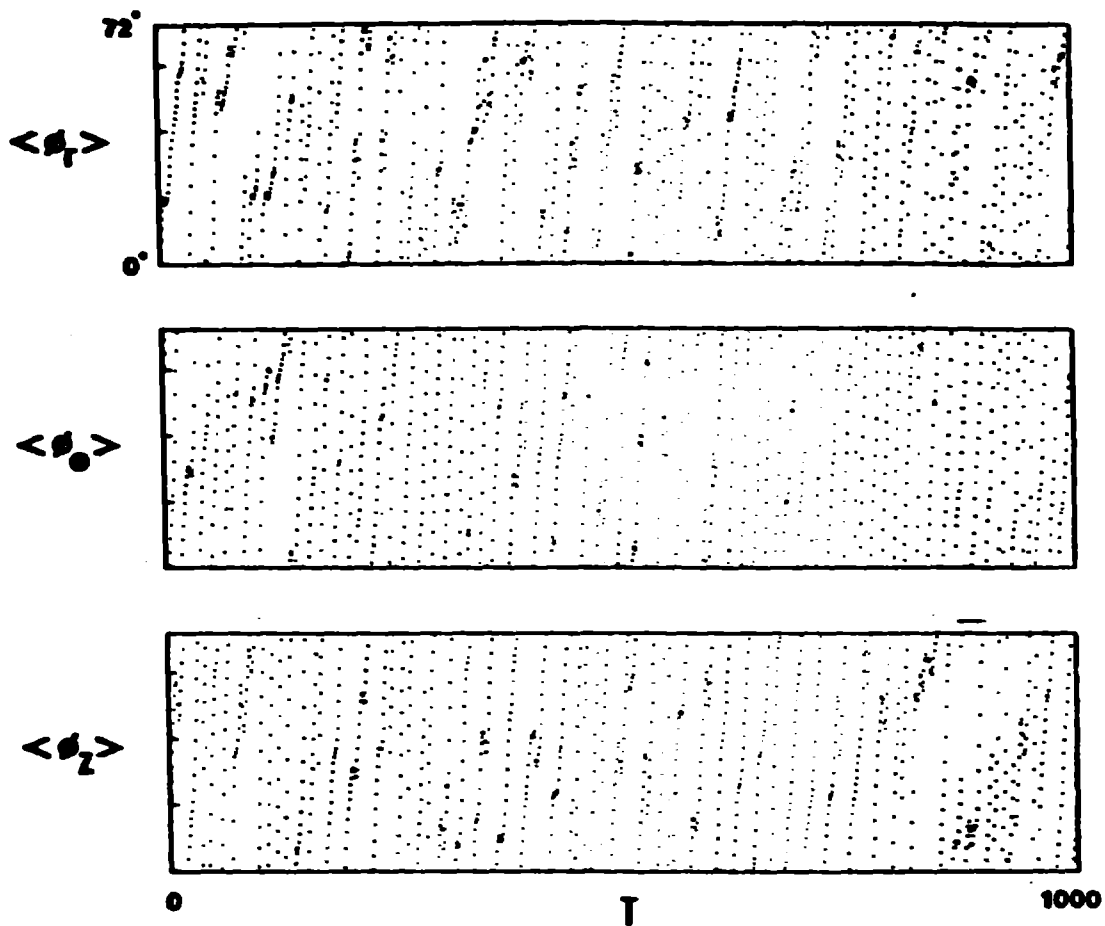Mean amplitudes versus time for run KRGA ($l = 5$).

Figure 30.

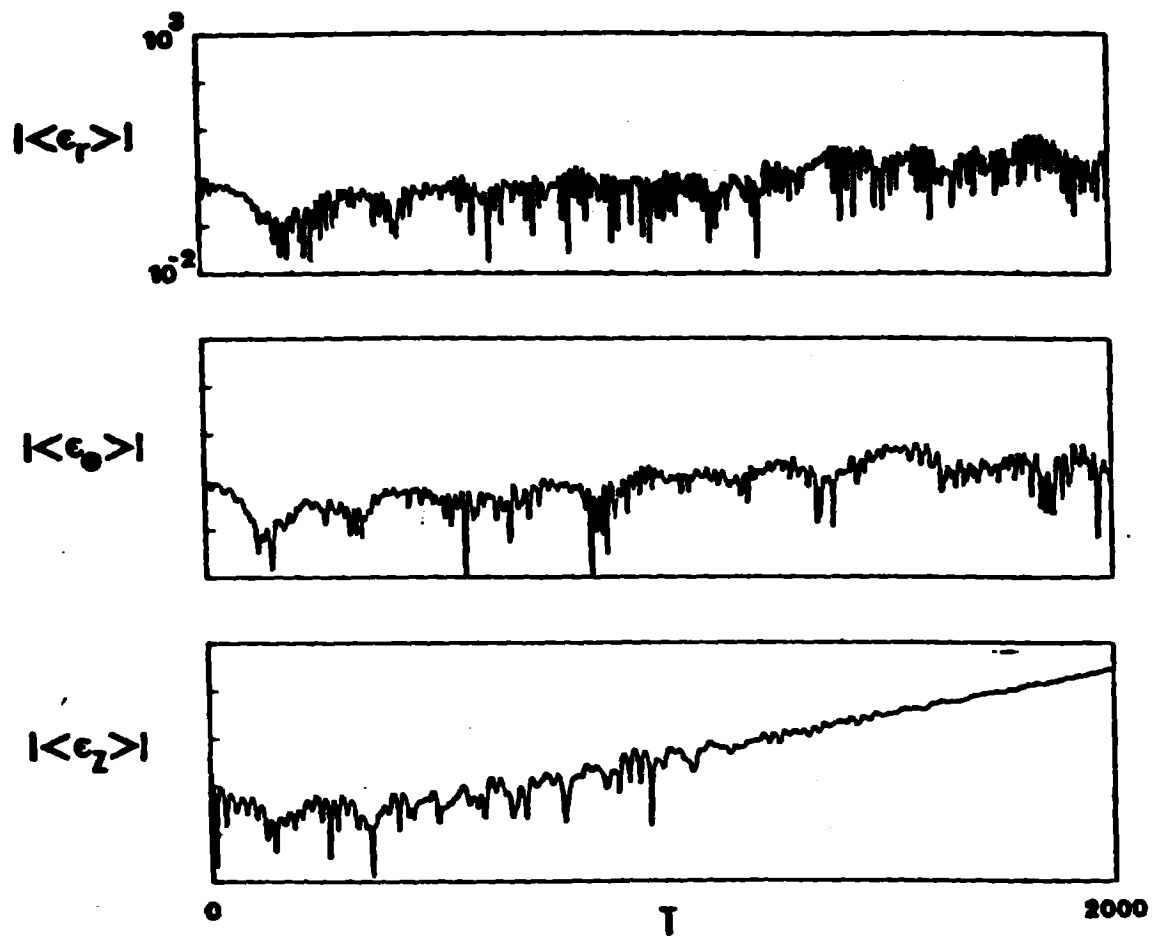Mean phases versus time for run KRGA ($l = 5$).

Figure 31.

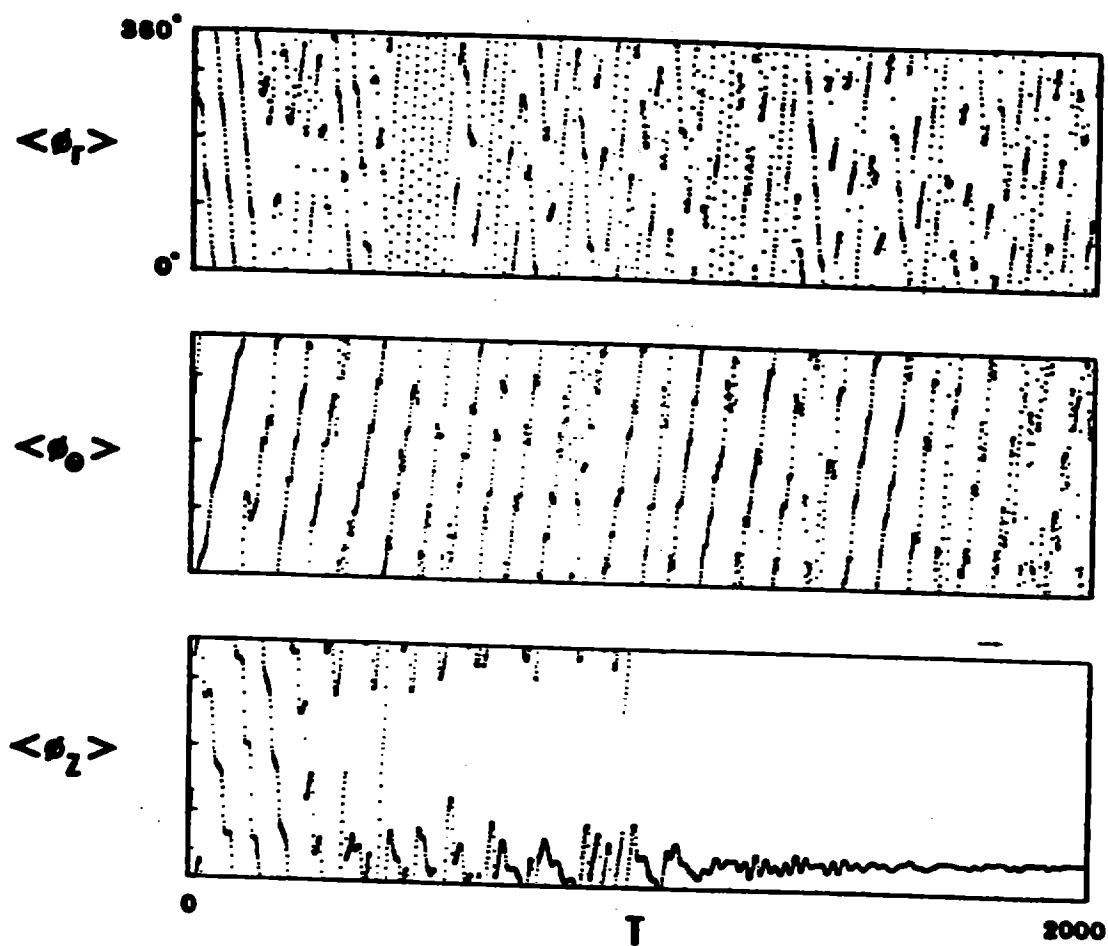Mean amplitudes versus time for run KRDA/B ($l = 1$, denser plasma background).

Figure 32.

Mean phases versus time for run KRDA/B ($l = 1$, denser plasma background).